Fabrication of Bi^{3+} substituted yttrium aluminum iron garnet (YAIG) nanoparticles and their structural, magnetic, optical and electrical investigations

Rameshwar B. Borade, S. B. Kadam, Devendra S. Wagare, R. H. Kadam, Sagar E. Shirsath, S. R. Nimbore & A. B. Kadam

Journal of Materials Science: Materials in Electronics

ISSN 0957-4522
Volume 30
Number 22

J Mater Sci: Mater Electron (2019)
30:19782-19791
DOI 10.1007/s10854-019-02344-3

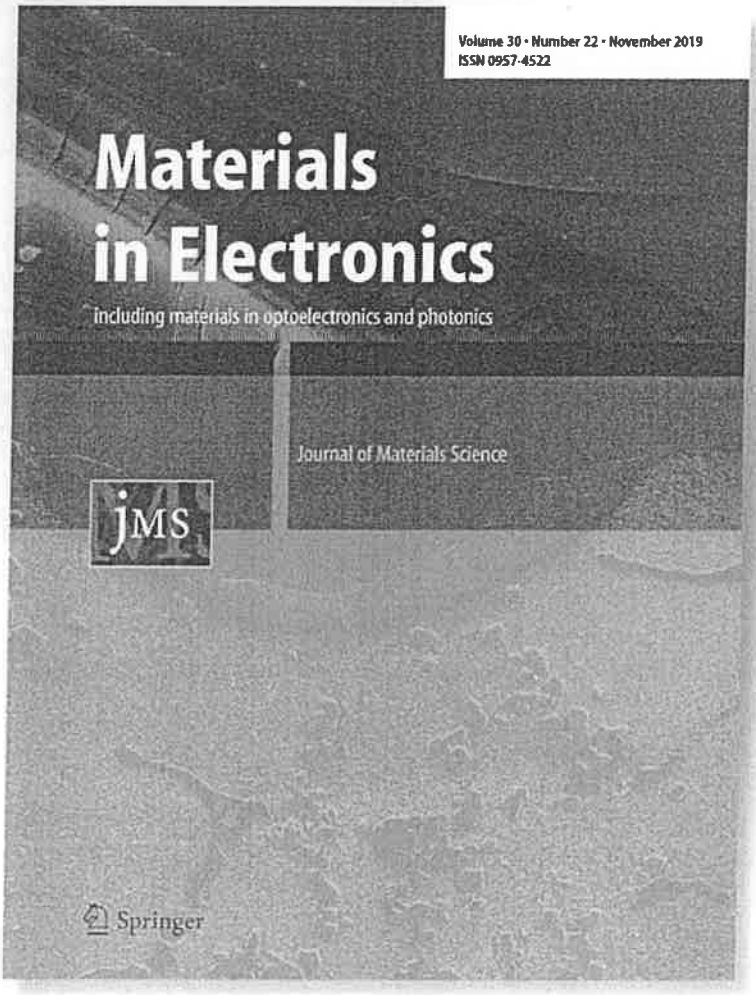

Springer

Journal of Materials Science: Materials in Electronics (2019) 30:19782–19791
https://doi.org/10.1007/s10854-019-02344-3

Fabrication of Bi^{3+} substituted yttrium aluminum iron garnet (YAIG) nanoparticles and their structural, magnetic, optical and electrical investigations

Rameshwar B. Borade[1] · S. B. Kadam[2] · Devendra S. Wagare[3] · R. H. Kadam[4] · Sagar E. Shirsath[5] · S. R. Nimbore[6] · A. B. Kadam[1]

Received: 22 June 2019 / Accepted: 3 October 2019 / Published online: 17 October 2019

Abstract
In this work, $Y_{3-x}Bi_xAl_{0.5}Fe_{4.5}O_{12}$ nanoparticles in powder form with composition x = 0.0, 0.5, 1.0,1.5 and 2.0 were fabricated by a sol–gel auto-combustion technique and calcined at 1150 °C for 10 h. The analysis of X-ray diffraction patterns using Rietveld refinement suggests that Bi-substituted yttrium aluminum iron garnet (YAIG) samples crystallize in cubic structure with Ia-$\bar{3}$d space group. The average size of crystallite of the samples calculated by the Scherer formula is found in the range of 19–24 nm which are in consistent with that of measured from Williamson–Hall curve. The absorption bands in Infrared spectra corresponding to garnet are shift to lower frequency with the increase of the Bi^{3+} concentration. Raman spectroscopy shows the non-vibrational behavior of Bi-substituted YAIG due to the excitation of Y^{3+} ions from the ground energy level. The morphology of the samples is observed by transmission electron microscopy and field emission scanning electron microscopy which showed most of the particles and grains are in spherical shape. The energy dispersive X-ray (EDS) spectra confirmed the elemental compositions of the selected sample. In UV–Visible spectroscopy, transparency of the samples decreases with increasing in Bi^{3+} ions substitution in YAIG. The saturation magnetization (Ms) decrease from the 14.59 to 2.25 emu/g with the increase in Bi^{3+} ions concentration, whereas, the values of coercivity (Hc) and retentivity (Mr) are very low. DC resistivity as a function of temperature shows the semiconducting nature of the synthesized samples and its decreased from 6.17×10^6 to 0.06×10^6 Ω-cm with the addition of Bi^{3+} ions.

1 Introduction

YIG and doped YIG's are ferrimagnetic materials which crystallizes in the cubic crystal structure with space group Ia$\bar{3}$d and having ionic distribution $[Y_3{}^{3+}]^c[Fe_2{}^{3+}]^a(Fe_3{}^{3+})^dO_{12}$. The rare earth Y^{3+} ions occupy the dodecahedral site having Wyckoff position 24c (1/8, 0, 1/4) and ferric ions Fe^{3+} resides at tetrahedral and octahedral sites having Wyckoff positions 24d (3/8, 0, 1/4) and 16a (0, 0, 0) respectively [1]. The magnetic properties of YIG depend on the site occupancy of the rare earth yttrium and iron ions among the different cation sites in the cubic crystal structure. The magnetic moments of the two Fe^{3+} ions in the a-site are aligned anti-parallel to those of the three Fe^{3+} ions in the d-site. Since the Y^{3+} ions in the c-sites are non-magnetic hence the resultant magnetic moment is due to the Fe^{3+} ions in the a- and d-sites. The strongest interactions occur between Fe^{3+} in 16(a) and 24(d) positions and between Fe^{3+} in 24(d) and a rare earth ion (M^{3+}) substituted for yttrium in 24(c) positions [2–4]. YIG is auspicious

✉ A. B. Kadam
drabkadam@gmail.com

1 Department of Physics, Jawahar Art Science and Commerce College, Andur, Osmanabad 413601, MS, India

2 Department of Physics, L.B.S. College, Partur, Jalna 431501, MS, India

3 Department of Chemistry, Vivekanand College, Samarth Nagar, Aurangabad 431001, India

4 Materials Science Research Laboratory, Shrikrishna Mahavidyalaya, Gunjoti, Osmanabad 413613, MS, India

5 School of Materials Science and Engineering, University of New South Wales, Kensington, Sydney, NSW 2052, Australia

6 Department of Physics, Arts, Commerce and Science College, Ashti, Beed 414203, MS, India

material for spintronic devices due to its excellent gyromagnetic, ferromagnetic and magneto-optical properties [5].

The different cations can be substituted in YIG at the dodecahedral site to change their structural and magnetic properties for the specific applications in different fields [6–8]. Wu et al. investigated the change in structural and magnetic properties by substituting the Lanthanum in YIG [9]. Arsad and Ibrahim [10] studied the effect of the Ce^{3+} ions on Dy doped yttrium iron garnet. They observed an increase of Ce contents in Dy doped YIG, the value of 'Ms' decreases, this is because of the weak ferromagnetic exchange interaction occurred between a and d sites. Lee et al. [11] observed that IR absorption bands of $Bi_xY_{3-x}Fe_5O_{12}$ (x = 0, 1, 2) shift according to Bi concentration.

YIG and substituted YIG are much attracting due to its applications in magneto-optical, microwave devices, lasers, and electrical devices. The replacement of Y^{3+} ions with the Bi^{3+} ions lower the annealing temperature for the formation of the YIG phase. However, Al^{3+} ion substitution in yttrium iron garnet decreases the magnetization which has potential applications in low microwave frequency devices [12, 13]. This result highlights on phase formation of Bi-substituted YAIG at lower annealing temperature and to decrease the magnetic parameters for their specific applications. Our main aim in this research is to synthesize $Y_{3-x}Bi_xAl_{0.5}Fe_{4.5}O_{12}$ nanoparticles with a high degree of substitution of bismuth using the sol–gel auto-combustion technique. It could be interesting to study the effect of Bi^{3+} addition on the properties of YAIG with replacement of Y^{3+} ions, and there is no literature available on such composition. Further, this is early attempt to study the structural, magnetic, optical, electrical and spectroscopic properties of Bi substituted YAIG ($Y_{3-x}Bi_xAl_{0.5}Fe_{4.5}O_{12}$; x = 0.0, 0.5, 1.0, 1.5 and 2.0) fabricated by the sol–gel auto-combustion technique which could be helpful for further research for device application.

2 Experimental procedure

2.1 Sample preparation

Yttrium (III) nitrate hexahydrate [$Y(NO_3)_3{\cdot}6H_2O$] (Sigma-Aldrich, 99.9%), Ferric(III) nitrate nonahydrate [$Fe(NO_3)_3{\cdot}9H_2O$] (Acros, 99.9%), Bismuth (III) nitrate pentahydrate [$Bi(NO_3)_3{\cdot}5H_2O$] (Acros, 99.9%), Aluminum nitrate nonahydrate (III) [$Al(NO_3)_3{\cdot}9H_2O$] (Acros, 99.9%) and citric acid monohydrate (Acros, 99.9%) were used for the synthesis of Bi-substituted aluminum doped YIG ($Y_{3-x}Bi_xAl_{0.5}Fe_{4.5}O_{12}$; x = 0.0, 0.5, 1.0, 1.5, 2.0) nanoparticles. The required amount of the nitrates with their weight proportion were dissolved and mixed in 100 mL distilled water to obtain the precursor solution of Bi-substituted YAIG. Citric acid was added to chelate $Y^{3+}$and Fe^{3+} in the solution. This mixture was continuously stirred using a magnetic stirrer and evaporated by heating at around 80–90 °C until the viscous gel was formed. The viscous gel heated at around 250 °C led to the combustion of the gel and converted into fine ash. The as-prepared samples were compressed in right-circular cylindrical pellets under 5-ton pressure. On the basis of thermo gravimetric analysis, all the samples were calcined at 1150 °C in air atmosphere for 10 h. The chemical reaction of these nitrates and citric acid which forming Bi-substituted YAIG is as bellow,

$$\begin{aligned}(3-x)\mathrm{Y}\left(\mathrm{NO_3}\right)_3\cdot 6\mathrm{H_2O} + x\mathrm{Bi(NO_3)_3}\cdot 5\mathrm{H_2O} \\ + 4.5\mathrm{Fe}\left(\mathrm{NO_3}\right)_3\cdot 9\mathrm{H_2O} + 0.5\ \mathrm{Al}\left(\mathrm{NO_3}\right)_3\cdot 9\mathrm{H_2O} \\ + 8\mathrm{C_6H_8O_7}\cdot \mathrm{H_2O} \rightarrow \mathrm{Y_{3-x}Bi_xAl_{0.5}Fe_{4.5}O_{12}} \\ + \mathrm{HNO_3}\uparrow + \mathrm{H_2O}\uparrow + \mathrm{CO_2}\uparrow\end{aligned} \quad (1)$$

2.2 Characterization

Room temperature XRD patterns were used to study the structural parameter by employing Rietveld refinement with the help of Fullprof software. Morphology, grain size, and shape of the synthesized samples were studied by FE-SEM (MIRA-3 LMH, JEOL JSM-6360) and transmission electron microscopy (TEM, Philips CM-200). The composition and stoichiometry of the middle sample was determined by EDAX(INCA Oxford, attached to the FE-SEM). Room temperature magnetic hysteresis loops of the samples for applied fields 2 T were recorded by vibrating sample magnetometer (VSM). The variation of DC resistivity with temperature for the samples was carried out by using two probe experimental set-up.

3 Result and discussion

3.1 Structural analysis

The XRD pattern (black solid circle) with Rietveld refined data (red solid line) of Bi-substituted YAIG nanoparticles is shown in Fig. 1. All the samples crystallize in cubic YAIG with space group Ia-$\bar{3}$d. It is observed from Fig. 1 that the single phase YAIG is formed for x = 0.0 and x = 0.5, whereas for x > 0.5 YAIG is formed with some mixed phases of Bi_2O_3 and YBFO ($Y_nBi_{1-n}FeO_3$). In Bi-substituted YIG, secondary phases were observed when bismuth has excessive composition [11, 14]. The typical reliability Rietveld refinement factors like expected R-factors (R_{exp}) and weighted profile R-factors (R_{wp}) are summarized in Table 1. The lattice parameter (a) refined from the Rietveld refinement is given in Table 1. The lattice

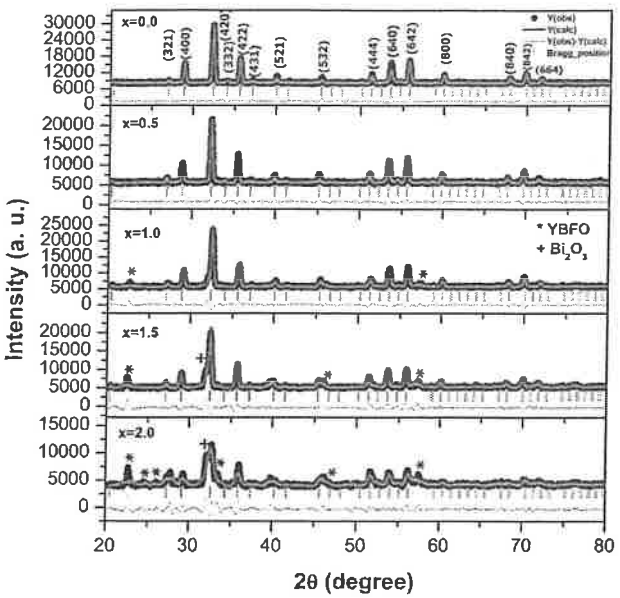

Fig. 1 Rietveld refined XRD patterns of $Y_{3-x}Bi_xAl_{0.5}Fe_{4.5}O_{12}$ powder samples annealed at 1150 °C for 10 h

parameter increases from 12.34 to 12.37 Å for x = 0.5, this is due to the difference in size of Bi^{3+} and Y^{3+} ions. For x > 0.5, the lattice parameter decreases randomly due to the secondary phases observed in the XRD pattern.

The crystallite sizes of the Bi-substituted YAIG were calculated from the most intense peak (420) of XRD data and by employing Debye–Scherer equation [15]:

$$D = \frac{K\lambda}{\beta \cos\theta} \tag{2}$$

where β is full width at half maximum intensity, λ is a wavelength of incident X-ray and K is shape factor having value of 0.9. The values of crystallite size with respect to the Bi concentration are given in Table 1. It is observed that crystallite size increases for x = 0.5. Furthermore, crystallite size decreases with increasing Bi concentration. The average crystallite size of the samples was in the range of 19–24 nm.

3.2 Williamson–Hall analysis

In order to investigate the microstrain in the prepared samples, strain and size of the nanoparticles was measured by the Williamson–Hall method assuming uniform deformation model (UDM). The strain induced in nanocrystals was calculated by the formula [16]:

$$\varepsilon = \frac{\beta}{4\tan\theta} \tag{3}$$

From Eqs. (2) and (3), total broadening can be written as

$$\beta = 4\varepsilon \tan\theta + \frac{K\lambda}{D\cos\theta} \tag{4}$$

This equation can be rewrite as

$$\beta\cos\theta = 4\varepsilon \sin\theta + \frac{K\lambda}{D} \tag{5}$$

On the basis of these equations, we have determined 4sinθ versus βcosθ (Fig. 2). The slope of 4sinθ versus βcosθ gives the strain induced and y-intercept gives the size of the nanocrystals of Bi-substituted YAIG. The values of strain and crystallite size measured from the W–H curve are listed in Table 1. For x = 0.0, a line of fit is approximately parallel to the X-axis which reflects the absence of microstrain in the sample. For rest of the samples, the slope of the line of fit is positive which shows the tensile strain induced in the crystal of the Bi-substituted YAIG samples. The values of tensile strain are increase from ε = 0 to 16.5×10^{-4} with the increase in Bi^{3+} ions in YAIG. This is because of the substitution of Bi^{3+} ions having a larger ionic radius than the Y^{3+} ions in YAIG which expanding the crystal lattices [16]. The size of crystallite measured from the y-intercept for pure YAIG is 22.40 nm and then it increases for x = 0.5 up to 23.58 nm. The increase of crystallite size is due to the enhancement of crystallinity or growth of crystal by the substitution of Bi^{3+} ions for this composition [17]. For x ≥ 1.0, crystallite size decreases with the increase in the Bi composition due to the presence of secondary phases or solubility limit of Bi in YAIG. Values of crystallite size estimated from the W–H

Table 1 Structural parameters obtained from Rietveld Refinement and Geometric parameters of $Y_{3-x}Bi_xAl_{0.5}Fe_{4.5}O_{12}$ (x = 0.0, 0.5, 1.0, 1.5, 2.0) nanoparticles

Composition (x)	Lattice parameter (Å)	R_{exp}	R_{wp}	Crystallite size (nm)		Strain $\varepsilon \times 10^{-4}$
				Scherrer formula	W–H method (UDM)	
0.0	12.34	7.32	19.7	22.90	22.40	0
0.5	12.37	8.48	22.9	23.39	23.58	1.52
1.0	12.32	7.77	23.7	21.24	21.40	1.80
1.5	12.33	7.74	29.8	19.17	20.70	1.95
2.0	12.26	4.08	18.3	18.26	20.60	16.8

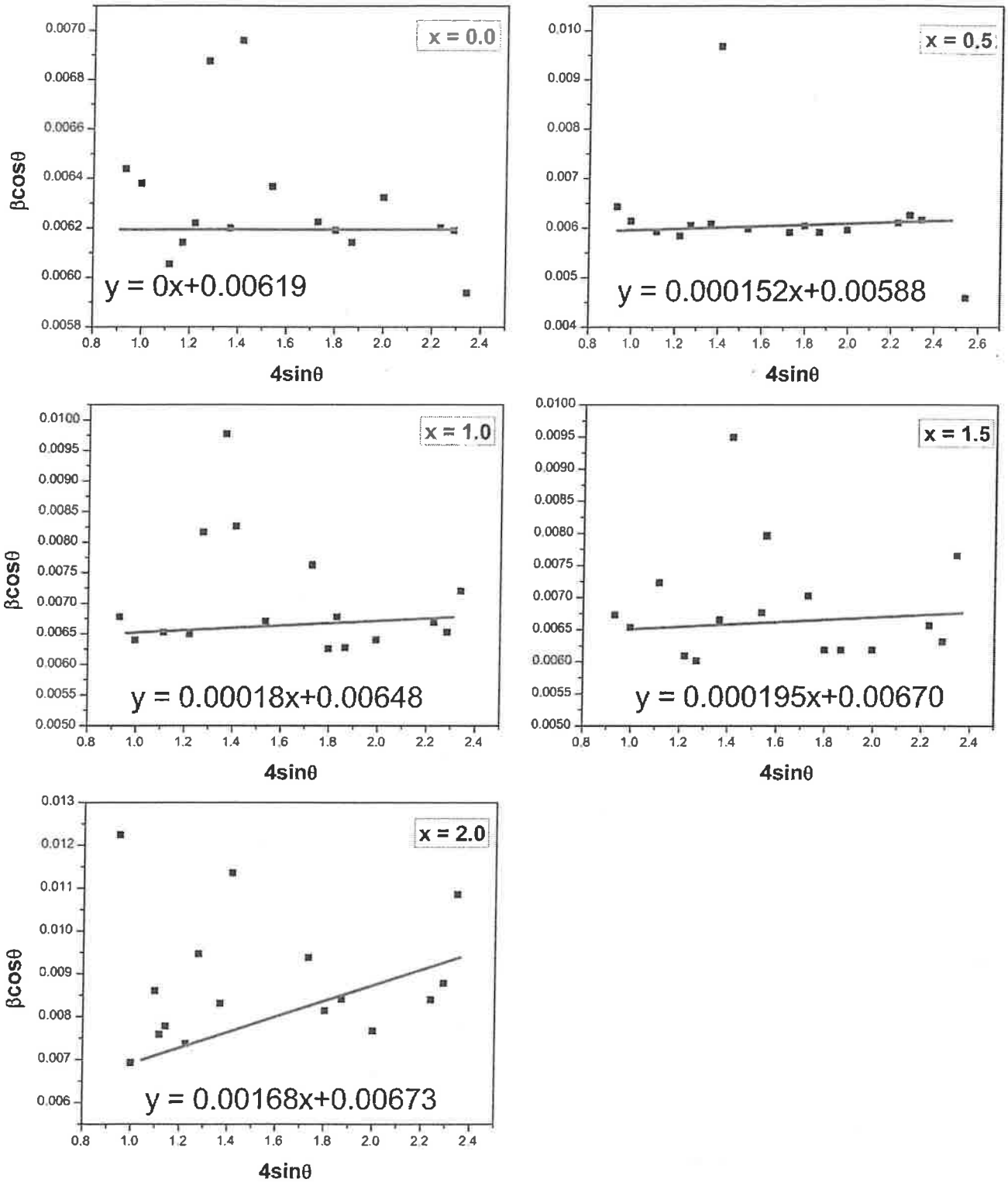

Fig. 2 Williamson–Hall plots for $Y_{3-x}Bi_xAl_{0.5}Fe_{4.5}O_{12}$ nanoparticles to estimate the strain and crystallite size assuming UDM

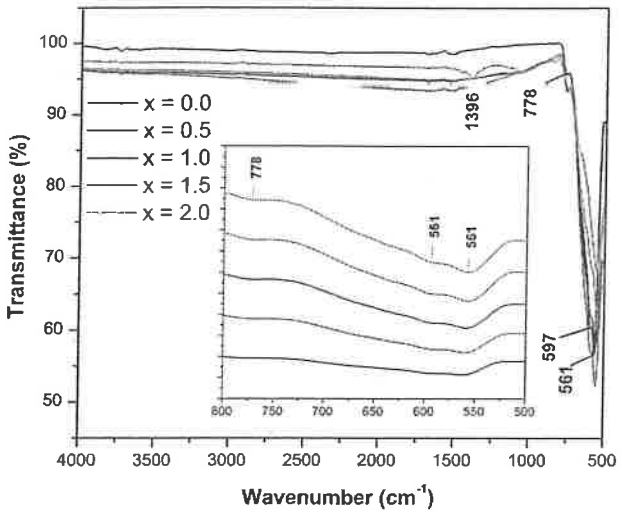

Fig. 3 FT-IR spectra of $Y_{3-x}Bi_xAl_{0.5}Fe_{4.5}O_{12}$ powder samples

curve are in good agreement with values calculated from the Scherer formula.

3.3 Spectroscopic analysis

Figure 3 shows FTIR transmittance spectra of the $Y_{3-x}Bi_xAl_{0.5}Fe_{4.5}O_{12}$ powders which were measured in the range of 500–4000 cm^{-1} at room temperature. These FT-IR spectra shows three absorption peaks at 561, 597, 778 cm^{-1} for x = 0.0. This high-frequency band is ascribed to the vibration in the tetrahedral Fe–O bond. The absorption bands corresponding to a garnet shift to lower frequency with an increase of Bi^{3+} concentration. These absorption bands appeared at 558, 594, 775 cm^{-1} for x = 2.0. The shift of peak towards lower frequency is due to the decrease in the Fe–O bond strength [18]. A peak observed around the 1400 cm^{-1} is related to the NO^{3-} radicals. These results are consistent with our observation of the XRD analysis that shows a structural transition in YIG as a function of Bi^{3+} concentration.

Raman spectra of Bi-substituted YAIG samples measured at room temperature are shown in Fig. 4a and b. There are 25 allowed Raman active modes in yttrium iron garnet according to group theory [19]. Figure 4a shows the Raman spectra in the range of 50 to 4000 cm^{-1} for different composition of Bi^{3+} ions in YAIG. Approximately all Raman active modes present in all the prepared samples. All the samples show a broad band around 2200 to 3300 cm^{-1} with few maximum intensity peaks. These high-intensity peaks are located at 2670, 2866 and 3025 cm^{-1} for x = 0.0, whereas for x > 0.0, intensity of peaks decreases with increasing Bi^{3+} ions in YAIG. This is the non-vibrational behavior of Bi-substituted YAIG due to the excitation of Y^{3+} ions from the ground energy level. The similar results of non-vibrational behavior are observed in lanthanide sesquioxides and ugrandite garnet due to the excitation of different ions [20, 21]. Figure 4b shows the expanded view of Raman spectra in the range of from 100 to 900 cm^{-1} for different composition of Bi^{3+} ions in YAIG. The peak observed around 273 cm^{-1} is associated with internal vibrations of the molecular group FeO_4. The peak observed at 273 cm^{-1} for x = 0.0 is due to the translational motion of dodecahedral site. This peak shift towards lower frequency from 273 to 272 cm^{-1} for x = 0.5, whereas for x > 0.5, peak shifts towards the higher

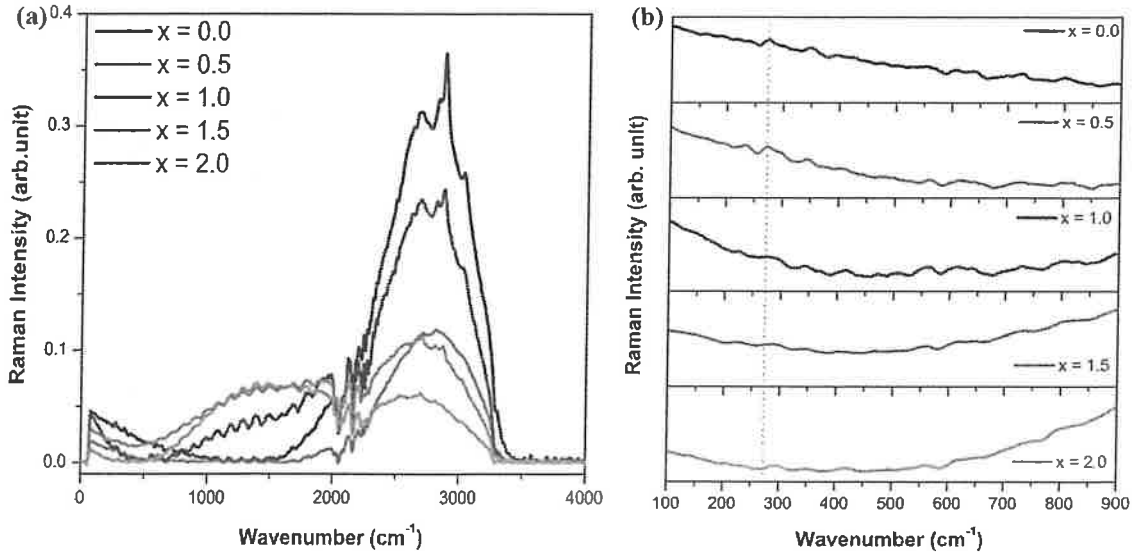

Fig. 4 **a** FT-Raman spectra, **b** expanded plots of $Y_{3-x}Bi_xAl_{0.5}Fe_{4.5}O_{12}$ powder sample

frequency from 272 to 292 cm^{-1}. This behavior is related to the variation in lattice parameter which increases for x = 0.5 and decreased thereafter with Bi-concentration.

3.4 Morphological analysis

The typical FE-SEM image of the prepared $Y_2Bi_1Al_{0.5}Fe_{4.5}O_{12}$ powder revealed its phase and microstructure. The morphology and its corresponding EDAX spectra of the middle sample (x = 1.0) are shown in Fig. 5 a and b respectively. The average grain sizes of the nanoparticles observed from the FE-SEM image are in the range of 300–400 nm. The particle size depends on different factors such as sintering temperature, porosity and grain boundary [22]. The image of the sample exhibits most of the grains are spherical in shape.

The chemical composition and stoichiometric proportions of the typical samples of $Y_2Bi_1Al_{0.5}Fe_{4.5}O_{12}$ garnet nanoparticles were confirmed by energy dispersive analysis (EDAX). The spectrum verified the existence of elements Fe, Y, O, Bi and Al which is an evidence for phase of Bi-substituted YAIG. The compositional percentage of all the ions obtained by the EDAX pattern is shown in the inset of EDAX figure. From this inset table, it is clear that the theoretical and observed atomic percentage of Y^{3+}, Bi^{3+}, Al^{3+}, Fe^{3+}, and O^{2-} are in close agreement with each other. All the elements exist in $Y_2Bi_1Al_{0.5}Fe_{4.5}O_{12}$ are in good stoichiometric proportions with an error of 2–3%.

To get more insight on the morphology of the prepared Bi-substituted YAIG samples, the TEM image of the middle sample (x = 1.0) is shown in Fig. 6. The particles observed from TEM are agglomerated and it is difficult to estimate the exact particle size and shape. However, the particle sizes observed from TEM are within the range of 90–150 nm. The process of agglomeration of particles is due to the magnetic interaction among the nanoparticles [23] since yttrium iron garnet is a ferromagnetic material.

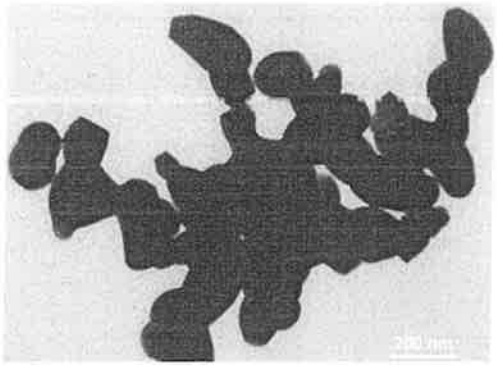

Fig. 6 TEM image of $Y_2Bi_1Al_{0.5}Fe_{4.5}O_{12}$

3.5 Optical properties

The transmittance spectra of Bi-substituted YAIG for all the samples are shown in Fig. 7a by converting absorbance data and using Beer's law, $I = I_0e^{-\alpha t}$ [24]. Figure 6a shows that the transmittance is close to 30% in the ultraviolet region for pure YAIG. In visible region, it decreases to 8%. Transparency of the samples decreases with increasing the Bi^{3+} ions in YAIG due to the roughness and irregular grain boundary [25].

Figure 7b shows the variation of absorption coefficient squared as with photon energy to determine the optical band gap energy of nanoparticles. The optical band gap energy for x = 0.0 is 4.03 eV, it decreases to 3.75 eV for x = 0.5 due to the intrinsic electronic transitions in the lattice [26–28]. After x = 1.0, it again increases with the increase in Bi-substitution. This non-linear behavior may be due to the secondary phase observed at the higher concentration of Bi in YAIG.

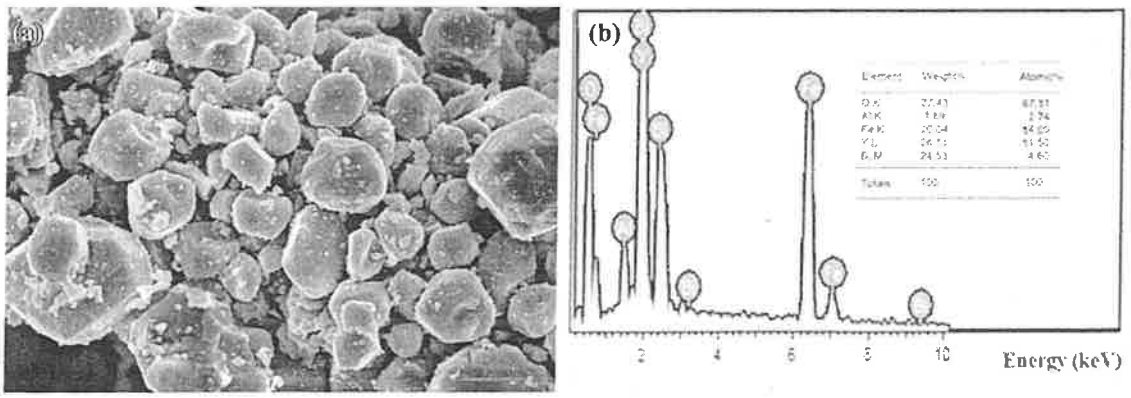

Fig. 5 a FE-SEM image and b energy dispersive X-ray spectroscopy spectra of $Y_2Bi_1Al_{0.5}Fe_{4.5}O_{12}$

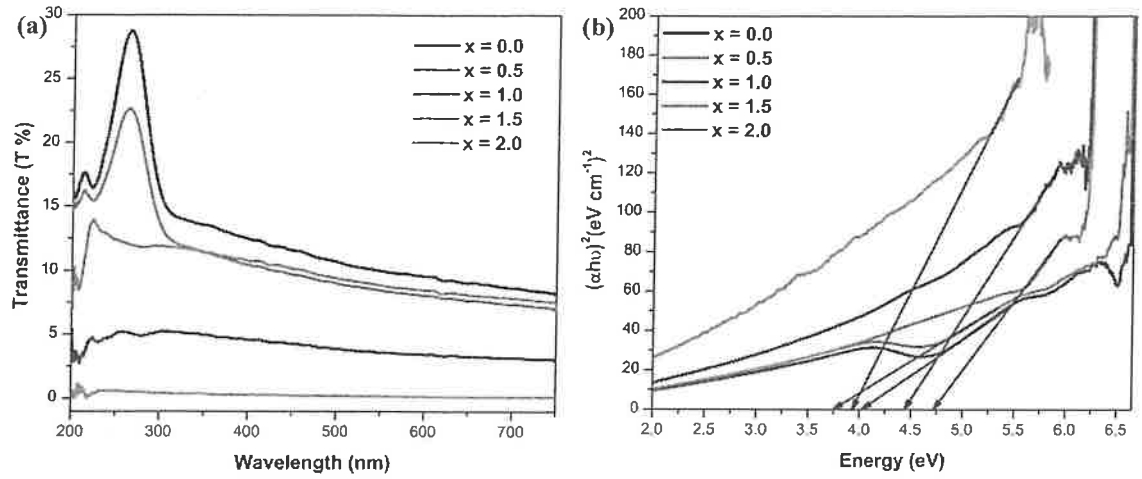

Fig. 7 a Optical transmittance spectra with respect to wavelength, b absorption coefficient squared as a function of photon energy of $Y_{3-x}Bi_xAl_{0.5}Fe_{4.5}O_{12}$

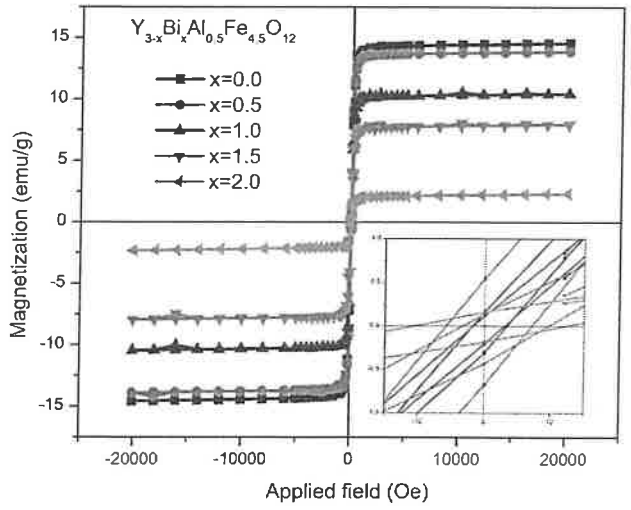

Fig. 8 Magnetic hysteresis loops of $Y_{3-x}Bi_xAl_{0.5}Fe_{4.5}O_{12}$ powder sample annealed at 1150 °C for 10 h

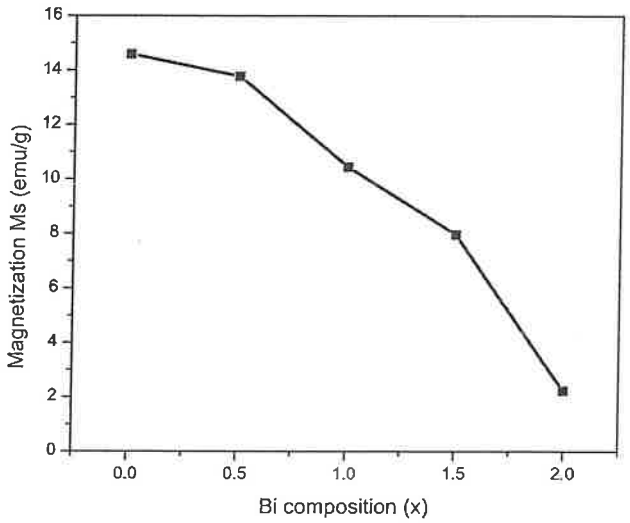

Fig. 9 Variation of saturation magnetization (Ms) with Bi concentration

3.6 Magnetic properties

In order to study the Bi^{3+} substitution effect on the magnetic properties of YAIG, M-H hysteresis loops were recorded by using the vibrating sample magnetometer under the applied magnetic field of 2 T at room temperature. Figure 8 shows the hysteresis loops for all the samples have fine narrow 's' shape which indicates the soft magnetic behavior. Figure 9 shows the variation of saturation magnetization with the Bi concentration. The Saturation magnetization (Ms) decreases from 14.59 to 2.25 emu/g with the increase in Bi^{3+} concentration in YAIG. The substitution of Bi^{3+} into Y^{3+} changes the magnetic structure of the sample. The Bi^{3+} ions prefer the dodecahedral sites and Al^{3+} ions prefer the tetrahedral sites. Thus, ionic distribution structure can be represented by $[Y^{3+}_{3-x}\ Bi^{3+}]c[Fe_2{}^{3+}]a(Fe^{3+}_{4.5}\ Al^{3+}_{0.5})dO_{12}$. In this distribution, both Y^{3+} and Bi^{3+} ions are non-magnetic ions which indicate that the substitution does not change the number of magnetic sub-lattices. The Bi^{3+} substitution will distort the magnetic structure of Fe^{3+} ions on octahedral a-sites and tetrahedral d-sites because of the radius of Bi^{3+} (1.17 Å) is larger than the radius Y^{3+} (0.9 Å). Magnetic properties of garnet materials are largely depend upon the super-exchange interactions and cation position [29–31]. The strongest super-exchange interactions occur in Fe^{3+} (*a*)—O^{2-}–Fe^{3+} (*d*) which is a common feature of all iron garnets. The microscopic structure distortion on a- and d-sites decreases the super-exchange interaction. The decrease in super-exchange

Table 2 Saturation magnetization, coercivity, remanence magnetization and magneton number for $Y_{3-x}Bi_xAl_{0.5}Fe_{4.5}O_{12}$ (x = 0.0, 0.5, 1.0, 1.5, 2.0) nanoparticles

Composition (x)	Saturation magnetization (emu/g)	Coercivity (Oe)	Remanence magnetization	magneton number (n_B)
0.0	14.59	1.8069	0.18	1.89
0.5	13.78	5.7920	0.55	1.93
1.0	10.44	1.6584	0.12	1.58
1.5	07.97	3.2920	0.16	1.29
2.0	02.25	10.5940	0.16	0.39

interaction decreases the saturation magnetization. This result is similar to Gd-YIG [32] and Tb-YIG [33].

Saturation magnetization, coercivity (Hc), remanence magnetization (Mr) and magneton number (n_B) are listed in Table 2. It is found that coercivity and remanence magnetization of all the samples are very low. The values of coercivity lie between 1.8 and 10.6 Oe and remanence magnetization lies in 0.12–0.55 emu/g. The Bohr magneton number 'n_B' (saturation magnetization per formula unit in Bohr magneton in μ_B of the synthesized samples is calculated with the help of saturation magnetization value (M_s) obtained from hysteresis loop [34].

$$n_B = \frac{molecular\ weight\ XM_s}{5585} \quad (6)$$

The values of Bohr magneton number (shown in Table 2) are decreases with increase in Bi^{3+} ions in YAIG due to the decrease in magnetic interaction.

3.7 Electrical properties

The nanoparticles of $Y_{3-x}Bi_xAl_{0.5}Fe_{4.5}O_{12}$ (x = 0.0, 0.5, 1.0, 1.5, 2.0) were pressed into a circular pellet of dimensions ~ 10 mm × 4 mm. For good Ohmic contact, silver paste was surfaced on both the faces of pellets. The DC resistivity for all the prepared garnet samples was measured in the temperature range of 300–700 K using two-probe experimental setup. Figure 10 shows the variation of DC resistivity with respect to temperature for all the composition of Bi-substituted yttrium aluminum iron garnet samples. The graph shows that electrical DC resistivity decreases with temperature for all the samples which reflects the semiconducting behavior. The DC resistivity of the garnet samples decreases from 6.17×10^6 to 0.06×10^6 Ω-cm with increasing the Bi^{3+} ion substitution in YAIG. The temperature dependence of DC electrical resistivity is according to the hopping conduction mechanism [35, 36], which attribute the increase in conductivity due to the electron hopping between the charge carriers. Substituted non-magnetic Bi^{3+} ions in place of Y^{3+} take part in the conduction process. The hopping process

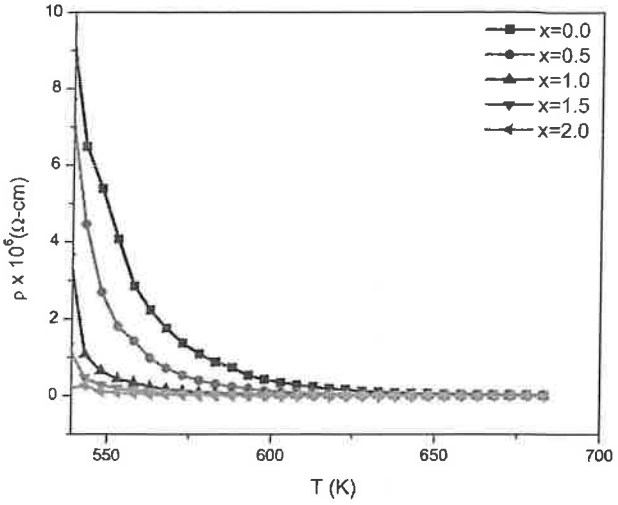

Fig. 10 Variation of electrical resistivity (ρ) with temperature (T) of $Y_{3-x}Bi_xAl_{0.5}Fe_{4.5}O_{12}$

between the Fe^{2+}/Fe^{3+} and between the Bi^{2+}/Bi^{3+} increases [37]. Thus, conductivity increases and the DC electrical resistivity decrease.

4 Conclusions

Rietveld refinement shows that it is possible to replace Y^{3+} ions by the Bi^{3+} ions in yttrium aluminum iron garnet up to the composition x = 0.5. After this composition, secondary phases are observed due to the solubility limit of Bi^{3+} ions in yttrium aluminum iron garnet. In this study, single phase Bi-substituted YAIG is formed for $x \leq 0.5$, whereas a weak Bi_2O_3 phase along with another secondary phase of YBFO are observed for x > 0.5. The calculated average crystallite size of nanoparticles was estimated within the range of 19–24 nm. Values of crystallite size estimated from the W–H curve are good agreement with the values calculated from the Scherer formula. The characteristics IR spectra of YAIG shift towards the lower frequency shows the Bi^{3+} ions effect on YAIG. The nanoparticles observed from FE-SEM and TEM shows Bi-YAIG produced in nano-sized form. Values of Ms are decreased with Bi concentration due to the occurrence of weak ferromagnetic exchange interaction between a–d sites, which is ascribed to the lattice distortion in the crystal. Values of 'Hc' and 'Mr' are very low suggesting soft ferrimagnetic nature. The variation in DC resistivity with temperature shows the semiconducting nature for each sample and it decreases with the increase in Bi^{3+} ion substitution in YAIG, and is related to the hopping process of ions. The samples with $x \lesssim 1.0$ exhibit outstanding properties such as high crystallization, soft magnetic nature, optical,

and electrical properties which have potential application for communication, microwave, and magneto-optical devices.

Acknowledgements Authors are thankful to Tata Institute of Fundamental Research (TIFR), Mumbai and SAIF, Indian Institute of Technology Madras (IITM), Chennai for providing the VSM and FT-Raman measurement facilities.

References

1. B. Deka, S. Ravi, D. Pamu, Impedance spectroscopy and ac conductivity mechanism in Sm doped yttrium iron garnet. Ceram. Int. **43**, 10468–10477 (2017)
2. T.C. Mao, J.C. Chen, Influence of the addition of CeO_2 on the microstructure and the magnetic properties of yttrium iron garnet ceramic. J. Magn. Magn. Mater. **302**, 74–81 (2006)
3. S. Geller, J. Remeika, R. Sherwood, H. Williams, G. Espinosa, Magnetic study of the heavier rare-earth iron garnets. Phys. Rev. **137**, A1034 (1965)
4. D. Rodić, A. SzytuŁa, Z. Tomkowicz, M. Guillot, H. Le Gall, Temperature dependence of lattice constants and thermal expansion coefficient of terbium-yttrium ferrites garnets. J. Magn. Magn. Mater. **75**, 79–87 (1988)
5. L. Liu, Y. Suwa, S. Sato, Y. Nakasone, M. Nishi, G.T. Dang, E.K. Pradeep, T. Kawaharamura, Incorporation of yttrium to yttrium iron garnet thin films fabricated by mist CVD. Jpn. J. Appl. Phys. **56**(4S), 42 (2017)
6. R.B. Borade, S.E. Shirsath, G. Vats, A.S. Gaikwad, S.M. Patange, S.B. Kadam, R.H. Kadam, A.B. Kadam, Polycrystalline to preferred-(100) single crystal texture phase transformation of yttrium iron garnet nanoparticles. Nanoscale Adv. **1**(1), 403–413 (2019)
7. X. Haitao, H. Yang, X. Wui, Yu. Lianxiang, Magnetic properties of Bi-doped $Y_3Fe_5O_{12}$ nanoparticles. Curr. Appl. Phys. **8**, 1–5 (2008)
8. L. Jin, Y. Wang, L. Guangduo, J. Li, Y. He, Z. Zhong, H. Zhang, Temperature dependence of spin-wave modes and Gilbert damping in lanthanum-doped yttrium-iron-garnet films. AIP Adv. **9**, 025301 (2019)
9. H. Wu, F. Huang, T. Xu, R. Ti, X. Lu, Y. Kan, X. Lv, W. Zhu, J. Zhu, Magnetic and magnetodielectric properties of Y_{3-x} La x Fe_5O_{12} ceramics. J. Appl. Phys. **117**(14), 144101 (2015)
10. A. Arsad, N. Ibrahim, The effect of Ce doping on the structure, surface morphology and magnetic properties of Dy doped-yttrium iron garnet films prepared by a sol–gel method. J. Magn. Magn. Mater. **410**, 128–136 (2016)
11. H. Lee, Y. Yoon, H. Yoo, S.A. Choi, K. Kim, Y. Choi, H. Melikyan, T. Ishibashi, B. Friedman, K. Lee, Magnetic and FTIR studies of Bi_xY_{3-x} Fe_5O_{12} (x = 0, 1, 2) powders prepared by the metal organic decomposition method. J. Alloys Compd. **509**, 9434–9440 (2011)
12. Aakansha, S. Ravi, Structural, magnetic and dielectric properties of Cr substituted yttrium iron garnets. J. Am. Ceram. Soc. **101**(11), 5046–5060 (2018)
13. O. Opuchovic, S. Culunlu, A.U. Morkan, I.A. Morkan, D. Niznansky, E. Garskaite, A. Beganskiene, A. Kareiva, Structural, morphological, and magnetic characterization of bulk and thin films Y_3Al_{5-x} Fe x O_{12} (YAIG): from the perspective of aqueous sol–gel processing. Chem. Eng. Commun. **204**(9), 1037–1048 (2017)
14. K. Matsumoto, K. Yamaguchi, T. Fujii, A. Ueno, Preparation of bismuth-substituted yttrium iron garnet powders by the citrate gel process. J. Appl. Phys. **69**, 5918–5920 (1991)
15. V.K. Mande, D.N. Bhoyar, S.K. Vyawhare, K.M. Jadhav, Effect of Zn^{2+}–Cr^{3+}substitution on structural, morphological, magnetic and electrical properties of $NiFe_2O_4$ ferrite nanoparticles. J. Mater. Sci. **29**, 15259–15270 (2018)
16. C. Murugesan, G. Chandrasekaran, Impact of Gd^{3+} substitution on the structural, magnetic and electrical properties of cobalt ferrite nanoparticles. RSC Adv. **5**, 73714–73725 (2015)
17. R. Tholkappiyan, K. Vishista, Tuning the composition and magnetostructure of dysprosium iron garnets by Co-substitution: an XRD, FT-IR, XPS and VSM study. Appl. Surf. Sci. **351**, 1016–1024 (2015)
18. P.B.A. Fechine, E.N. Silva, A.S. de Menezes, J. Derov, J.W. Stewart, A.J. Drehman, I.F. Vasconcelos, A.P. Ayala, L.P. Cardoso, A.S.B. Sombra, Synthesis, structure and vibrational properties of $GdIG_X$:YIG1-x ferrimagnetic ceramic composite. J. Phys. Chem. Solids **70**, 202–209 (2009)
19. R. Peña-Garcia, A. Delgado, Y. Guerra, G. Duarte, L.A.P. Gonçalves, E. Padrón-Hernández, The synthesis of single-phase yttrium iron garnet doped zinc and some structural and magnetic properties. Mater. Res. Express **4**, 016103 (2017)
20. T. Biljan, S. Roncevic, Z. Meić, K. Kovač, Non-vibrational features in NIR FT-Raman spectra of lanthanide sesquioxides. Chem. Phys. Lett. **395**, 246–252 (2004)
21. T. Moroz, A. Ragozin, D. Salikhov, G. Belikova, V. Puchkov, H. Kagi, Micro-Raman spectra of ugrandite garnet. Spectrochim. Acta A. **73**, 436–439 (2009)
22. X.H. Wang, P.L. Chen, I.W. Chen, Two-step sintering of ceramics with constant grain-size, I. Y_2O_3. J. Am. Ceram. Soc. **89**, 431–437 (2006)
23. S.M. Asgarian, S. Pourmasoud, Z. Kargar, A. Sobhani-Nasab, M. Eghbali-Arani, Investigation of positron annihilation lifetime and magnetic properties of $Co_{1-x}CuxFe_2O_4$ nanoparticles. Mater. Res. Express **6**(1), 015023 (2018)
24. F.W. Aldbea, N.I. Ahmad, N.B. Ibrahim, M. Yahya, Effect of increasing pH value on the structural, optical and magnetic properties of yttrium iron garnet films prepared by a sol–gel method.". J. Sol-Gel. Sci. Technol. **71**, 31–37 (2014)
25. Y. Li, L. Xu, X. Li, X. Shen, A. Wang, Effect of aging time of ZnO sol on the structural and optical properties of ZnO thin films prepared by sol–gel method. Appl. Surf. Sci. **256**, 4543–4547 (2010)
26. M.C. Onbasli, L. Beran, M. Zahradník, M. Kučera, R. Antoš, J. Mistrík, G.F. Dionne, M. Veis, C.A. Ross, Optical and magneto-optical behavior of cerium yttrium iron garnet thin films at wavelengths of 200–1770 nm. Sci. Rep. **6**, 23640 (2016)
27. S.M. Peymani-Motlagh, A. Sobhani-Nasab, M. Rostami, H. Sobati, M. Eghbali-Arani, M. Fasihi-Ramandi, M.R. Ganjali, M. Rahimi-Nasrabadi, Assessing the magnetic, cytotoxic and photocatalytic influence of incorporating Yb 3+ or Pr 3+ ions in cobalt–nickel ferrite. J. Mater. Sci. **30**(7), 6902–6909 (2019)
28. A. Sobhani-Nasab, M. Behpour, M. Rahimi-Nasrabadi, F. Ahmadi, S. Pourmasoud, New method for synthesis of $BaFe_{12}O_{19}/Sm_2Ti_2O_7$ and $BaFe_{12}O_{19}/Sm_2Ti_2O_7$/Ag nano-hybrid and investigation of optical and photocatalytic properties. J. Mater. Sci. **30**, 5854–5865 (2019)
29. L. Wang, Z. Huang, H. Zhang, R. Yu, Phase and magnetic properties evolutions of Y3–x (CaZr)xFe5 – xO12 by the sol–gel method. J. Magn. Magn. Mater. **395**, 73–80 (2015)
30. M. Rahimi-Nasrabadi, M. Behpour, A. Sobhani-Nasab, S.M. Hosseinpour-Mashkani, $ZnFe_{2-x}La_xO_4$ nanostructure: synthesis, characterization, and its magnetic properties. J. Mater. Sci. **26**(12), 9776–9781 (2015)
31. M. Rahimi-Nasrabadi, M. Behpour, A. Sobhani-Nasab, M.R. Jeddy, Nanocrystalline Ce-doped copper ferrite: synthesis, characterization, and its photocatalyst application. J. Mater. Sci. **27**(11), 11691–11697 (2016)

32. Z. Cheng, H. Yang, L. Yu, Y. Cui, S. Feng, Preparation and magnetic properties of $Y_3Fe_5O_{12}$ nanoparticles doped with the gadolinium oxide. J. Magn. Magn. Mater. **302**, 259–262 (2006)
33. F.W. Aldbea, N.B. Ibrahim, M.H. Abdullah, R.E. Shaiboub, Structural and magnetic properties of Tb x Y 3–x Fe 5 O 12 ($0 \leq x \leq 0.8$) thin film prepared via sol–gel method. J. Sol-Gel Sci. Technol. **62**(3), 483–489 (2012)
34. S.E. Shirsath, S.S. Jadhav, B. Toksha, S. Patange, K. Jadhav, Influence of Ce^{4+} ions on the structural and magnetic properties of $NiFe_2O_4$. J. Appl. Phys. **110**, 013914 (2011)
35. R. Kadam, A. Biradar, M. Mane, S.E. Shirsath, Sol-gel auto-combustion synthesis of $Li3_xMnFe_{2-x}O_4$ and their characterizations. J. Appl. Phys. **112**, 043902 (2012)
36. M. Ajmal, A. Maqsood, Influence of zinc substitution on structural and electrical properties of $Ni_{1-x}Zn_xFe_2O_4$ ferrites. Mater. Sci. Eng. B **139**, 164–170 (2007)
37. Y.-J. Siao, X. Qi, C.-R. Lin, J.-C. Huang, Dielectric relaxation and magnetic behavior of bismuth-substituted yttrium iron garnet. J. Appl. Phys. **109**, 07A508 (2011)

ISSN 2229-4406

International Registered & Recognized
Research Journal Related To Higher Education for all Subjects

UNIVERSAL RESEARCH ANALYSIS

(UGC Approved & Peer Reviewed Research Journal)

Year - IX, Issue - XVII, Vol.- IV | Impact Factor 5.35 (GRIFI) | Sept. 2018 To Feb. 2019

EDITOR IN CHIEF

Prof. Jarachand Yadav

IMPACT FACTOR
5.35

ISSN 2229-4406

UGC Approved International Registered & Recognized
Research Journal Related to Higher Education for all Subjects

UNIVERSAL RESEARCH ANALYSIS

UGC APPROVED & PEER REVIEWED RESEARCH JOURNAL

Issue - XVII, Vol. IV
Year - IX (Half Yearly)
Sept. 2018 To Feb. 2019

Editorial Office :
'Gyandev-Parvati',
R-9/139/6-A-1,
Near Vishal School,
LIC Colony,
Pragati Nagar, Latur
Dist. Latur - 413531.
(Maharashtra), India.

Contact : 02382 -241913
9423346913 / 9503814000
9637935252 / 7276301000

Website
www.irasg.com

E-mail :
interlinkresearch@rediffmail.com
visiongroup1994@gmail.com
mbkamble2010@gmail.com

Publisher :
Jyotichandra Publication
Latur, Dist. Latur - 413531. (MS)

Price : ₹ 200/-

INDEX

4

Human Development Index: An Overview

N.N. Nanwate
Arts Commerce &Science College,
Ashti, Dist. Beed

Dr. S.R. Nimbore
Principal,
Arts Commerce &Science College,
Ashti, Dist. Beed

Research Paper - Economics

Introduction:

The UNDP has developed a set of composite indices such as human development index (HDI), Human Poverty Index (HPI) and Gender related Development Index (GDI) for measuring the level of development and disparities among the countries in the world. The true aim of development is not only to boost incomes, but also to maximize human choices— by enhancing human rights, freedoms, capabilities and opportunities and by enabling people to lead long, healthy and creative lives. Critical to this process is work central to human existence. Human beings prepare for work as children, engage in work as adults and expect to retire from work in later life. Through the human lifecycle, quality of life is thus closely bound to the quality of work. The idea central to the first HDR published in 1990 was that 'people are the real wealth of a nation'. Development was seen as more than just economic growth and was taken to encompass the development of the people of a country. A new vision of development was envisaged by Mahbub-ul Haq and Amartya Sen who emphasized the need to 'put people at the center' of all development efforts and Setting the Framework the necessity to enlarge people's choices by providing them with the means to lead an educated, healthy life with a decent standard

erview

R. Nimbore
Principal,
rce &Science College,
ti, Dist. Beed

as human development
velopment Index (GDI)
countries in the world.
so to maximize human
id opportunities and by
to this process is work,
hildren, engage in work
human lifecycle, quality
entral to the first HDR
on'. Development was
mpass the development
visaged by Mahbub-ul-
ple at the center' of all
enlarge people's choices
fe with a decent standard

of living. "Plural principles such as equity, sustainability and respect for human rights are thus key.

Human development is all about human freedom freedom to realize the full potential of every human life not just of a few nor most but of all lives in every of the world. Over the past quarter century the world has changed and with it the development land scape new countries have emerged and our planet is now home than 7 billion people one in four of them young .

Progress in human development has been impressive over the past 25 year. People now live longer more children are in school and more people have access to basic social services .The millennium development declaration and commitments at the turn of the century to end basic human deprivations within 15 years added to the momentum.

Human development is a process of enlarging people choices .But human development is also the objective so it both process and an outcomes. Human development implies that people must influence the process that shape their lives. In all this economics growth is an important means to human development but not the end .Human development is the development of the people throughbuilding human capability by the people thought active participation in the process that shape their lives and for the people by improving their lives. It is border than approach the basic needs human resourcesapproach.

Objective of the study:

1) To understand the human development index
2) To know the HDI in India
3) To study the Indicators of HDI

Definition of HDI:

Mahbub – ul- Haq, one of the architect and refiner of Human Development concept said that the basic purpose of development is to enlarge people's choices. People often value achievements that do not show up at all, or not immediately, in income or growth figures: greater access to knowledge, better nutrition and health services, more secure livelihoods, security against income and physical violence, satisfying leisure hours, political and cultural freedoms and sense of participation in community activities. Thus the objectiveness of development is to create on enabling environment for people to enjoy

long, healthy and creative lives. Human development is to create on enabling environment for people to enjoy long, healthy and creative lives. Human development is about people, about expanding their choices to lead lives they value. "Human development is a process of enlarging people's choices. In principle, these choices can be infinite and change over time. But at all levels of development, the three essential ones are for people to lead a long and healthy life, to acquire knowledge and to have access to resources needed for a decent stand of living.

India's HDI value and rank

India became independent in 1947, Jawaharlal Nehru stressed the importance of the task that lay ahead of ending poverty, ignorance, disease and inequality of opportunity. As the 1st Five Year Plan (FYP) was launched, it however did not spell out any specic planning strategy linking sectorial investment proposals to the objective of the plan. But in the 2nd FYP the principles of 'socialistic pattern of society' underlay the planning strategy and emphasized social gain. It put stress on raising standards of living by raising National income through a rapid The human development (HD) story of India is unique in its kind. Through the preparation of not only national, but also sub-national Human Development Reports (HDR), India has decentralized and integrated the human development concept into its development agenda at national, State, as well as district and municipality level. More sub-national HDRs have been produced in India than in any other country. More HDRs have been produced in India than the total number of Global HDRs. A disti nctive feature of the HDR preparation process is the ûrm State ownership, and multi -stakeholder partnerships. This has enabled policy dialogue on crucial HD issues.

The national average HDI for India in 2008 was 0.467.By 2010, its average HDI had risen to 0.519. UNDP, the sponsor of Human Development Index methodology since 1990, reported India's HDI to be 0.554 for 2012, an 18% increase over its 2008 HDI. United Nations Declared India's HDI is 0.586 in 2014, an 5.77% increase over 2012. As for the year 2016, HDI for India stood at 0.624.HDI is composite index that takes into consideration (1) Life expectancy, (2) Education and (3) Per capita income. India climbed one spot to 130 out of 189 countries in the latest human development rankings released today by the United Nations Development Programme (UNDP). India's HDI

enabling environment
pment is about people,
velopment is a process
ıfinite and change over
ıre for people to lead a
resources needed for a

ɔssed the importance of
ıequality of opportunity.
ıot spell out any specic
ective of the plan. But in
lay the planning strategy
ving by raising National
ıdia is unique in its kind.
al Human Development
an development concept
t and municipality level.
any other country. More
)bal HDRs. A disti nctive
ip, and multi -stakeholder
ɜsues.
67.By 2010, its average
ment Index methodology
% increase over its 2008
, an 5.77% increase over
I is composite index that
3) Per capita income. India
an development rankings
me (UNDP). India's HDI

value for 2017 is 0.640, which put the country in the medium human development category. Between 1990 and 2017, India's HDI value incased from 0.427 to 0.640, an increase of nearly 50 percent – and an indicator of the country's remarkable achievement in lifting millions of people out of poverty. Norway, Switzerland, Australia, Ireland and Germany lead the ranking, while Niger, the Central African Republic, South Sudan, Chad and Burundi have the lowest scores in the HDI's measurement of national achievements in health, education and income. Within South Asia, India's HDI value is above the average of 0.638 for the region, with Bangladesh and Pakistan, countries with similar population size, being ranked 136 and 150 respectively. India's HDI value for 2015 is 0.624—which put the country in the medium human development category—positioning it at 131 out of 188 countries and territories. Between 1990 and 2015, India's HDI value increased from 0.428 to 0.624, an increase of 45.7 percent. Table A reviews India's progress in each of the HDI indicators. Between 1990 and 2015, India's life expectancy at birth increased by 10.4 years, mean years of schooling increased by 3.3 years and expected years of schooling increased by 4.1 years. India's GNI per capita increased by about 223.4 percent between 1990 and 2015.

Indicators of Human Development Index (HDI):

The three criteria or indicators which represent different aspects of good life or the three goals of human development are:

1. Longevity:

It is measured by life expectancy at birth. Life expectancy at birth means how many years a newly born infant can hope to live in this world. This represents element of health in the Human Development Index (HDI).

2. Education or Knowledge:

It is measured by the weighted average of adult literacy and mean years of schooling. For this 2/3rd weight is given to adult literacy and 1/3rd weight is given to the mean years of schooling.

3. Standard of Living:

It is measured by real per capita income of a country at purchasing power parity (PPP) prices that is, adjusted for purchasing power of currencies of different countries.

Let us explain how Human Development Index (HDI) is estimated for different countries There are three goals of development, namely, better health as measured by life expectanc at birth, better education or knowledge as measured by literacy rate and standard c living as measured by per capita income measured in terms of purchasing power parit prices (PPP) in US dollars.

For example, for life expectancy at birth the range is 25 to 82 years, for literac rate the range is 0 to 100 per cent and for per capita income the range is $ 100 to 40,00 in terms of PPP (US $). The value of each component of human development index i calculated by using the following formula –

HDI for individual component = (Actual Value – Minimum Value) / (Maximu Value –Minimum Value)If the actual value of an individual variable in HDI of a country equal to the minimum, the index of that variable for a country is zero. On the other han if the value of an individual component is equal to the maximum value, the index of th component will be equal to one. For example, India's life expectancy at birth in 2011 w 65.5, the life expectancy index for India according to the above formula (with the give range of 25-85) will be-Life expectancy Index of India = (65.5–25) / (85 – 25) 0.673Similarly, with 3460 PPP (US $) of India's per capita income, its individual inde (with range 100-40,000) = (Yj– YÀ)2 = 0.084 Constructing overall HDI we take avera of three individual indexes with each having 1/3 weight. Thus, HDI = 1/3 (per capi income index) + 1/3 (life expectancy index) + 1/3 (literacy index) after finding the valu of Human Development Index (HDI) for various countries they are ranked from th highest to the lowest.

Conclusion:

Policymakers need to ensure greater effectiveness of the existing social sect schemes on the HD formation process. Leakage in the schemes in terms of reaching o to the target groups is often noted, which must be avoided. Secondly, level of governan mechanism needs to be bettered by channelizing efficient utilization of allocated func There is a need for increasing both professionalism and responsiveness among the publ administration. PRIs have become an important arm of decentralized governance a can play a major role in this process, albeit with some reforms. Since the panchaya

for different countries.
ured by life expectancy
y rate and standard of
ırchasing power parity

to 82 years, for literacy
ange is $ 100 to 40,000
ı development index is

um Value) / (Maximum
ɔle in HDI of a country is
zero. On the other hand,
ı value, the index of that
ancy at birth in 2011 was
formula (with the given
65.5–25) / (85 – 25) =
ɔme, its individual index
rall HDI we take average
ıs, HDI = 1/3 (per capita
ĸ) after finding the values
hey are ranked from the

the existing social sector
:s in terms of reaching out
ɔndly, level of governance
ization of allocated funds.
siveness among the public
ntralized governance and
ms. Since the panchayats

mostly receive funds from the central government and such an external supply of funds tends to breed irresponsibility and corruption on the part of the PRIs, the PRIs can be empowered to raise resources on their own through the imposition of taxes and other such measures. They can also be granted more decision-making powers at the local level and their eligibility for obtaining Central funds could be linked to their competence in raising resources from internal sources. Simultaneously, participatory governance, through organizations of the marginalized groups (the landless, women, SHGs, Dalits, and Adivasis), along with the PRIs should be encouraged.

References :-

1) Sacchidananda Mukherjee1, Debashis Chakraborty and Satadru Sikdar(2014), Three Decades of Human Development across Indian States: Inclusive Growth or Perpetual Disparity? National Institute of Public Finance and Policy New Delhi.
2) Ambuj D.Sagar a,,Adil Najam(1998),The human development index: a critical review,Ecological Economics 25 249–264
3) Elizabeth A. Stanton (2007), The Human Development Index: A History, economic and political research institute.
4) UNDP (2010) Human Development in India: Analysis to Action Government of India.
5) A Sarvalingam and Marimuthu Sivakumar (2010) Human Development Measurement: A broader approach in India,MPRA Paper No. 22505, posted 5.
6) Hasan Al-Hilani 2012HDI as a Measure of Human Development: A Better Index than the Income Approach?IOSRJBM Volume 2, Issue 5.
7) Institute of Human Development (2010) Human development in India: Emerging issues and policy perspectives, icssr&World Bank. New Delhi.
8) www.HDI.India.in
9) www.UNDP report 2017.in
10) www.economics discussion.net

Studies on Synthesis and Structural Properties of Nickel Ferrite before and after Gamma Irradiation

Studies on Synthesis and Structural Properties of Nickel Ferrite before and after Gamma Irradiation

Santosh Kalunge[1], Anand Surase[2], D. R. Sapate[3], S. R. Nimbhore[4], V. K. Barote[5] and A. A. PAndit[1a)]

[1]Department of Physics, Yeshvantrao Chavan College of Arts, Commerce and Science, Sillod, Aurangabad - 431 004 (MS), India

[2]Department of Physics 2, New Arts, Commerce and Science College, Ahmednagar-414 001 (MS), India

[3]Department of Physics, Sant Ramdas Arts, Commerce and Science College, Ghansawangi, Jalna - 431 209 (MS), India

[4]Department of Physics, Adv B.D.Hambarde Mahavidyalaya Ashti, Beed – 414203 (MS), India

[5]Department of Physics Sant Dnyaneshwar Mahavidyalaya Soegaon, Aurangabad-431 120 (MS), India

a)Corresponding author email : yccsillod@yahoo.com

Abstract. In the present work nanocrystalline $NiFe_2O_4$ samples were prepared by the sol-gel auto combustion technique. The synthesis was carried out by taking citric acid as fuel with metal nitrate to fuel ratio as 1:3. The obtained powder was annealed at 550^{0}C for 4 h and then used for structural and magnetic investigations. Prepared nickel ferrite samples have been irradiated by gamma-ray (^{60}Co) to examine the changes that occurred in structural properties. Structural properties of nickel ferrite nanoparticles before and after gamma irradiation were carried out by X-ray diffraction (XRD) technique. From the XRD pattern, it was observed that all the Braggs planes reveal cubic spinel structure before and after gamma irradiation. A close examination of the XRD pattern revealed the crystallite size of 21 nm and 19 nm for nickel ferrite samples before and after gamma irradiation respectively. The obtained results help in providing interesting and useful study for various applications of nickel ferrites.

1. Introduction

Now-a-days magnetic materials are grabbing the attention of researchers and scientists because of their novel physicochemical properties [1]. Among magnetic materials, ferrites are the most attention-grabbing materials because of their magnetic and insulator properties [2, 3]. Among the various ferrites, nickel ferrites are vitally attributable to their astounding properties, such as high magnetic permeability, lower eddy current losses, and high resistivity making them a potential material for high-frequency applications [4-6].

The development of nanoscience and nanotechnology leads us to deal with and fabricating the material at nanoscale for a particular application. The unique characteristics of nanostructured materials are imported due to their changed electronic structure, close to that of an isolated atom or molecule [3]. Modifications and improvements of these materials are important to adjust the performance and efficiency of the different devices that use them. In recent times, in order to study the effect of irradiation on the properties of ferrite materials, fast heavy ions, laser beams, and gamma rays have been used [7]. Irradiation can be an effective tool to enhance crystal defects and adjust the properties of ferrite (soft and hard magnetic) in a controlled manner. A lot of scientific focus is thus given to the gamma-irradiation caused by the formation and alteration of defects leading to tunable structural and magnetic properties of ferrites. Radiation energy such as gamma rays interacts with materials (atomic electrons and atomic nuclei) [8, 9]. These interactions result in the scattering of particles, the excitation of electrons and vibrations (thermal), and the ionization of atoms, which usually cause interference in the material structure. This in turn modifies the material's electrical and magnetic properties [10, 11]. These improvements can be due to the breakage of ferrimagnetic ordering, surface-state pinning, and cation inversion, etc. Such modifications are quantitatively functions of the dose intensity of irradiation, dose duration, dose absorbed by the materials and quality of the target materials, etc [12, 13].

In the present study, we have carried out the synthesis of nickel ferrite by the sol-gel auto combustion method and irradiated with gamma-ray to understand the effect of gamma radiation on the structural properties of nickel ferrite.

2 Experimental

2.1 Materials

Synthesis of nickel ferrite was carried out by using chemicals such as ferric nitrate ($Fe(NO_3)_3\ 9H_2O$) nickel nitrate ($Ni(NO_3)_2\ 6H_2O$), citric acid ($C_6H_8O_7$), ammonia (NH_3), and distilled water. All the chemicals were used without further purification.

2.2 Preparation of nickel ferrite

The nickel ferrite nanopowder was prepared by using a cost-effective safe sol-gel auto combustion technique. To obtain better combustion citric acid was used as a chelating agent. The detailed procedure of sol-gel auto combustion is explained in our earlier reports [14, 15] The prepared fluffy powder was sintered at temperature 550 °C for 4 h using a muffle furnace to get a better crystalline nature and purity.

2.3 Characterization

The synthesized nickel ferrite samples were characterized by X-ray diffraction (XRD) technology to identify the crystalline phase. The Bruker D-8 X-ray diffractometer has a (2θ) angle range of $20\text{-}80^0$.

Results and Discussions

2.4 X-ray Diffraction

The X-ray diffraction pattern of nickel ferrite synthesized by the sol-gel auto- combustion method recorded at room temperature in 2θ range from $20\text{-}80^\circ$ showed in figure 1. The values of the lattice parameter of the prepared sample calculated by using the following relation [16, 17].

$$a = d_{hkl}\sqrt{h^2 + k^2 + l^2}$$

Where d is the interplanar spacing of two planes, 'a' is the lattice constant, and (hkl) is the miller indices. It revealed that the lattice parameter decreases after irradiation and caused increase in X-ray density.

$$d_B = \frac{m}{V}$$

Where, m is the mass and V is the volume ($\pi r^2 h$) of pallets. The obtained XRD patterns revealed the formation of the cubic spinel structure with Fd-3m space group. There is no impurity peak observed in the XRD pattern. The crystallite size of nickel ferrite before and after irradiation was found to be 21 nm and 19 nm respectively, which is calculated by using Debye-Scherrer's formula [18],

$$D = \frac{k\lambda}{\beta\cos\theta}$$

Where, k is the constant having value 0.89, λ is the X-ray light source wavelength (1.540 Å), β is full width at half maximum (FWHM) and θ is the glancing angle. The peak positions of the irradiated sample are shifted to the lower angle (2θ). The slight change of the reflective peaks in the irradiated samples is due to some induced disorder (compressive strain) in the crystal structure resulting from ion migration into interstitial positions. X-ray density (dx) of nickel ferrite was calculated by using the relation [19, 20],

$$d_x = {}^{8M}/_{N_A a^3}$$

Where dx is the X-ray density, M is the molecular weight of the composition, NA is the Avogadro's number and 'a' is the lattice constant. Calculated values of lattice constant, unit cell volume, average crystallite size, X-ray density, bulk density, the porosity of before and after irradiation of prepared nickel ferrite is tabulated in table 1.

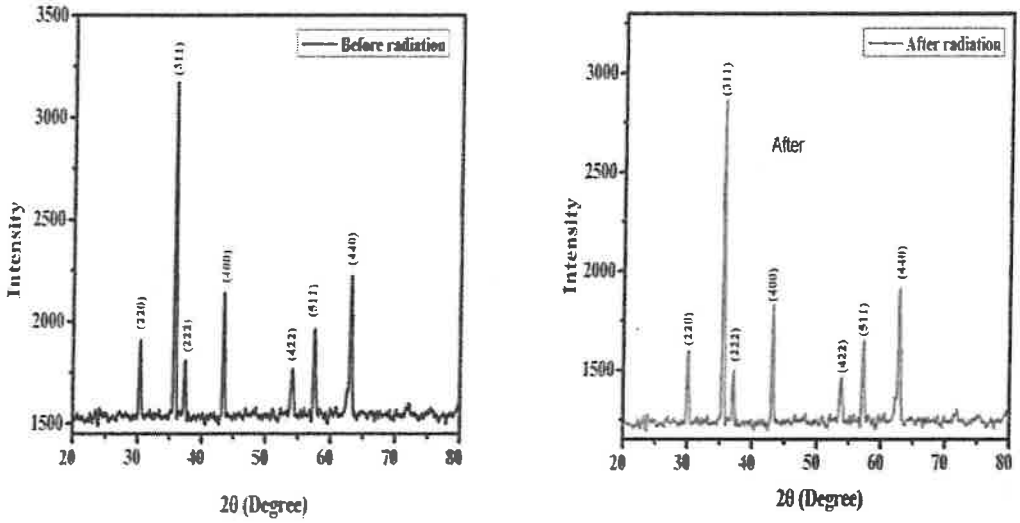

Figure 1. X-ray diffraction pattern of $NiFe_2O_4$ nanoparticles before and after radiation.

Table 1- Values of 'Lattice constant (a)', 'Unit cell volume (V)', 'Average crystallite size (D)', 'X-ray density (dX)', 'Bulk density (dB)', 'Porosity (P)' of nickel ferrites nanoparticles before and after gamma radiation

$NiFe_2O_4$	a (Å)	FWHM (Θ)	V	D (nm)	dx	d_B	Porosity %
Before radiation	8.336	0.3418	579.3	21.75	5.374	3.638	33.00
After radiation	8.329	0.3021	577.8	19.69	5.389	3.617	33.14

4. Conclusions

Nanostructured nickel ferrite sample was successfully prepared by the sol-gel auto-combustion method. The prepared ferrite sample was irradiated by ^{60}Co gamma-ray source. The XRD patterns confirmed the formation of cubic spinel ferrite with the Fd3m space group. The lattice parameter and crystallite size decreases after gamma irradiation.

Acknowledgement

One of the authors Kalunge, is thankful to Punyashlok Ahilyadevi Holkar University, Solapur for XRD facility and Government Institute of Science, Aurangabad for gamma irradiation facility.

References

1. Gul, S., et al., *A Comprehensive review of magnetic nanomaterials modern day theranostics.* Frontiers in Materials, 2019. **6**: p. 179.
2. Qian, K., et al., *The influence of Nd substitution in Ni–Zn ferrites for the improved microwave absorption properties.* Ceramics International, 2020. **46**(1): p. 227-235.
3. Besteiro, L.V., et al., *The fast and the furious: Ultrafast hot electrons in plasmonic metastructures. Size and structure matter.* Nano Today, 2019. **27**: p. 120-145.
4. Shukla, V., *Review of electromagnetic interference shielding materials fabricated by iron ingredients.* Nanoscale Advances, 2019. **1**(5): p. 1640-1671.
5. Harun-Or-Rashid, M., *Investigation of structural, morphological and electromagnetic properties of scandium doped nickel-copper-zinc ferrites.* 2019.
6. Barth, C.B., *High-density multilevel power converters for use in renewable and transportation applications.* 2019, University of Illinois at Urbana-Champaign.
7. Singh, P. and R. Kumar, *Radiation Physics and Chemistry of Polymeric Materials*, in *Radiation Effects in Polymeric Materials*. 2019, Springer. p. 35-68.
8. Wang, X.-X., et al., *Eco-mimetic nanoarchitecture for green EMI shielding.* Chemical Engineering Journal, 2019. **369**: p. 1068-1077.
9. Mande, V.K., et al., *Effect of γ-radiation on structural, morphological, magnetic and dielectric properties of Zn–Cr substituted nickel ferrite nanoparticles.* Journal of Materials Science: Materials in Electronics, 2019. **30**(1): p. 56-68.
10. Qiu, L., et al., *Enhancing the interfacial interaction of carbon nanotubes fibers by Au nanoparticles with improved performance of the electrical and thermal conductivity.* Carbon, 2019. **141**: p. 497-505.
11. Mino, L., et al., *Materials characterization by synchrotron x-ray microprobes and nanoprobes.* Reviews of Modern Physics, 2018. **90**(2): p. 025007.
12. Kumari, M., *Study the Effect of Gamma Irradiation on Structural and Electrical Properties of CdSe Nanowires.* 2018.
13. Angadi, V.J., et al., *Reduced A–B super exchange interaction in Sm 3+–Gd 3+-doped Mn–Zn ferrites due to high energy gamma irradiation.* Indian Journal of Physics, 2019. **93**(2): p. 169-174.
14. Kale, G., et al., *l-Ascorbic acid assisted synthesis and characterization of CoFe 2 O 4 nanoparticles at different annealing temperatures.* Journal of Materials Science: Materials in Electronics, 2016. **27**(2): p. 2151-2158.
15. Humbe, A.V., et al., *Nanocrystalline Ni 0.70− x Cu x Zn 0.30 Fe 2 O 4 with 0≤ x≤ 0.25 prepared by nitrate-citrate route: structure, morphology and electrical investigations.* Journal of Materials Science: Materials in Electronics, 2018. **29**(4): p. 3467-3481.
16. Routray, K.L., D. Sanyal, and D. Behera, *Gamma irradiation induced structural, electrical, magnetic and ferroelectric transformation in bismuth doped nanosized cobalt ferrite for various applications.* Materials Research Bulletin, 2019. **110**: p. 126-134.

17. Raut, A., et al., *Structural, electrical, dielectric and magnetic properties of Al 3+ substituted Ni-Zn ferrite.* Journal of Superconductivity and Novel Magnetism, 2016. **29**(5): p. 1331-1337.
18. Jadhav, S.A., et al., *Magneto-structural and photocatalytic behavior of mixed Ni–Zn nano-spinel ferrites: visible light-enabled active photodegradation of rhodamine B.* **Journal of** Materials Science: Materials in Electronics: p. 1-14.
19. Bharati, V., et al., *Influence of trivalent Al–Cr co-substitution on the structural, morphological and Mössbauer properties of nickel ferrite nanoparticles.* **Journal of Alloys and Compounds,** 2020. **821**: p. 153501.
20. Kounsalye, J.S., et al. *Structural, morphological and dielectric modifications in nanocrystalline Li 0.5 Fe 2.5 O 4 ferrites induced by high energy γ-irradiation.* **in** *Proceedings of the fourteenth biennial DAE-BRNS symposium on nuclear and radiochemistry: book of abstracts*. 2019.

Journal of Physics: Conference Series

Structural and dielectric properties of mixed spinel ferrite $Cu_{(0.7)}Zn_{(0.3)}Fe_2O_4$ nanoparticles

Structural and dielectric properties of mixed spinel ferrite $Cu_{(0.7)}Zn_{(0.3)}Fe_2O_4$ nanoparticles

S B Kale[1], R M Borade[2], J S Kounsalye[3] A V Raut[3], S R Nimbhore[3] and K M Jadhav[4]

[1]Department of Applied Sciences, Government Polytechnic College, Aurangabad 431004

[2]Department of Chemistry, The Institute of Science, Dr Homi Bhabha State University, Mumbai 400032

[3]Department of Physics, Late. R. B. Arts, Commerce and Smt. S. R. B. Science College, Arni, Dist. Yavatmal, India (MS)

[4]Department of Physics, Dr. Babasaheb Ambedkar Marathwada University, Aurangabad 431004 India

Corresponding author email : drjadhavkm@gmail.com

Abstract. In this communication we report structural and dielectric properties of mixed Cu-Zn spinel ferrite nanoparticles. $Cu_{(0.7)}Zn_{(0.3)}Fe_2O_4$ nanoparticles were synthesized by using standard and well known sol-gel auto-combustion techniques. The obtained nanoparticles were annulated at 520°C for 4 h and then used for further study. The X-ray diffraction (XRD) pattern was recorded at room temperature to investigate the single phase nanocrystalline nature of prepared sample. The XRD pattern shows formation of single phase cubic spinel structure with average crystallite size of ~24 nm. The crystallite size was determined by using standard Scherrer's equation. The other structural parameters like lattice constant, unit cell volume, X-ray density etc. were determined using XRD data. The dielectric properties were measured at room temperature and as a function of frequency using LCR-Q meter. The dielectric constant, dielectric loss and dielectric loss tangent all get decreased exponentially with increasing frequencies. The observed dielectric behaviour is similar to that of reported in the literature.

1. Introduction

Ferrites with iron oxide and metal oxide as a constituent magnetic materials are used in several technological applications [1]. They exhibit both kinds of properties that are ferromagnetic and electrical. They possess high electrical resistivity [2], low eddy current and dielectric loss, magnetization, high Curie temperature and therefore ferrites are known to be good magnetic and dielectric materials [3]. On account of their important electrical, dielectric and magnetic properties they are used in microwave devices [4, 5] high frequency applications, antenna rods [6, 7], memory

storage devices [8, 9] etc. These materials are continuously studied from last 7-8 decades because of their excellent twin properties of electrical insulator and magnetic conductor which can be improved by several ways. One of the important parameter for generating variations in the physical properties of the ferrite is the selection of synthesis method. Earlier, Ferrites were synthesized by ceramic technique [10], it has some inherent drawbacks. Some of the drawbacks are it requires high temperature, extended synthesis time and lack of technological approach. The drawbacks of ceramic method are overcomes with the help of wet chemical synthesis method. Some of the wet chemical method are sol-gel method [11, 12], sol-gel auto-combustion, co-precipitation [13, 14] , micro-emulsion [15] , hydrothermal [16] etc. All the wet chemical methods are advantages over the conventional ceramic method as they required low temperature for synthesis; the method yields high quality homogeneous powder. This method is simple and cost effective [17, 18], also this method requires least time as compared to the conventional ceramic method. This wet chemical method has gained an importance in the recent years. In this work, we have used the sol-gel auto combustion method for the synthesis of mixed $Cu_{(0.7)}Zn_{(0.3)}Fe_2O_4$ (CZK_7). Spinel ferrite with the chemical formula MFe_2O_4 (M = divalent cations like Cu, Zn, Co, Mn, Fe etc.) have cubic spinel structure with a space group Fd_3m [19, 20]. The spinel ferrite possesses two interstitial sites namely tetrahedral (A) and octahedral [B], in which contains of different valence and size can accommodate at appropriate site. Copper ferrite is a unique spinel ferrite and has tetragonal as well as cubic spinel structure dependently on the synthesis methods and conditions. Zinc (Zn^{2+}) is a divalent nonmagnetic cation can easily be incorporated in the lattice of copper ferrite. Thus, the mixed Cu-Zn spinel ferrite with the formula $Cu_{(0.7)}Zn_{(0.3)}Fe_2O_4$ (CZK_7) was prepared in the present study by well-known wet chemical method. The structural and dielectric properties were investigated by means of X-Ray diffraction and LCR-Q meter. The applied characterization techniques, structural and dielectric properties of $Cu_{(0.7)}Zn_{(0.3)}Fe_2O_4$ (CZK_7) ferrite nanoparticles are reported in this communication.

2. Experimental

2.1 Raw Materials

$Cu_{(0.7)}Zn_{(0.3)}Fe_2O_4$ (CZK_7) spinel ferrite nanoparticles have been prepared by sol-gel auto-combustion method in order to achieve homogeneous crystal structure. A stoichiometric proportion of metal nitrate solutions were used as a synthesis protocol. The purity, chemical strength and brand trust of these materials was checked for the laboratory synthesis of $Cu_{(0.7)}Zn_{(0.3)}Fe_2O_4$ (CZK_7) spinel ferrite nanoparticles. 99.9% pure AR graded ferric nitrate ($Fe(NO_3)_3 \cdot 9H_2O$) [21], copper nitrate ($Cu(NO_3)_2$) [22] and zinc nitrate ($Zn(NO_3)_2$) [23] was taken as a starting material for the present synthesis. Fuel plays an important role in sol-gel auto-combustion method, so we used citric acid ($C_6H_8O_7$) [24] as a fuel due to its wonderful complexing ability. Citric acid also has a low ignition temperature (200°C - 250°C) than that of the other fuels used in wet chemical methods

2.2 Synthesis Method

Beginning with the starting materials, metal nitrate to citric acid ratio was taken as 1:3 for the synthesis of $Cu_{(0.7)}Zn_{(0.3)}Fe_2O_4$ (CZK_7) spinel ferrite nanoparticles. The metal nitrates were stirred well with a drop by drop addition of liquid ammonium hydroxide (NH_4OH). An addition of ammonium hydroxide in metal nitrates helps to maintain the pH of the solution at 8. The mixed metal nitrate solution was stirred continuously and heated at 75 °C on a hot plate magnetic stirrer for 4 to 5 h. This step would helpful for the formation of sol in the reaction. Under the constant stirring and heating a transparent sol was heated at 100 °C for 1.5 h. On removal of water at some extend, small increase in temperature leads the reaction from transparent sol to a viscous brown gel. This viscous brown gel further transformed into a dried gel. Further, nitrate-citrate gel reaction takes place to dried gel formation which exhibited self-propagating combustion behaviour. At a particular temperature

ignition started and dry gel burnt in self-propagating combustion manner. The gel was burnt out completely and forms a loose powder of $Cu_{(0.7)}Zn_{(0.3)}Fe_2O_4$ (CZK_7) spinel ferrite. The obtained nanoparticles were annulated at 520°C for 4 h and then used for the further characterization.

3. Characterization

3.1 X-Ray Diffraction

The X-ray diffraction study of prepared $Cu_{(0.7)}Zn_{(0.3)}Fe_2O_4$ (CZK_7) spinel ferrite nanoparticles was performed on a Philips PW-1730 X-ray diffraction using Cu-kα radiation (λ = 1.5405 Å). The X-ray diffraction pattern was recorded in the 2θ range of 20°-80° at room temperature. Using XRD data various structural parameters were obtained.

3.2 Dielectric Properties

Dielectric properties of spinel ferrites are important because of their use in microwave applications. In the present study, dielectric properties of $Cu_{(0.7)}Zn_{(0.3)}Fe_2O_4$ (CZK_7) are studied by means of LCR-Q meter (Model HP 4284 A) as a function of frequency and at room temperature.

4. Results and discussion

4.1 Structural Properties

Figure 1 represents the room temperature XRD pattern of the $Cu_{(0.7)}Zn_{(0.3)}Fe_2O_4$ (CZK_7) sample. The reflections were identified as (111), (220), (311), (222), (400), (422), (511) and (400). These reflections were oriented at 2θ angles 18.218°, 30.057°, 35.418°, 38.669°, 43.101°, 53.442°, 56.942° and 62.506 angles respectively which reveals cubic spinel structure of $Cu_{(0.7)}Zn_{(0.3)}Fe_2O_4$ (CZK_7) [25]. These XRD has characteristics peaks matching with JCPDS card number PDF#340425. The values of Bragg's angle interplanar space and corresponding Miller Indices are given in the table 1.

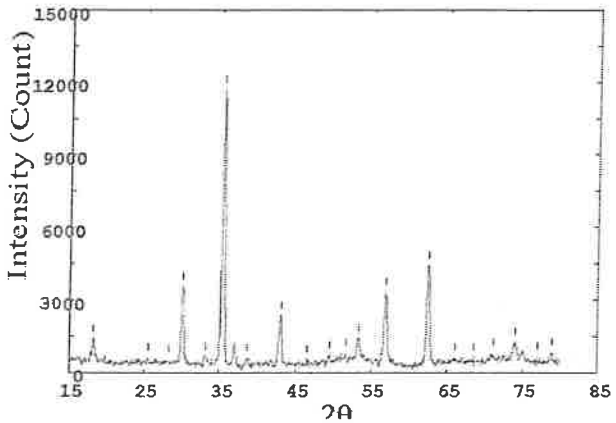

Figure 1. X-ray Diffraction pattern of $Cu_{(0.7)}Zn_{(0.3)}Fe_2O_4$ (CZK_7) spinel ferrite nanoparticles

The analysis of XRD data reveals that the prepared samples belongs to cubic spinel structure and is nanocrystalline in nature. The XRD data was used to evaluate various structural parameters like lattice constant, X-ray density etc..

The lattice constant of $Cu_{(0.7)}Zn_{(0.3)}Fe_2O_4$ (CZK_7) spinel ferrite nanoparticles was calculated from the formula [26] ;

$$a = d_{hkl}(h^2 + k^2 + l^2)^{\frac{1}{2}} \quad (1)$$

Where, d is interplanner spacing, hkl are the Miller indices and a is lattice constant. From the XRD data (FWHM of strongest Bragg's reflection (311) oriented at 2θ = 35.418°) was considered to calculate crystallite size (t) using Scherrer's formula [27];

$$t = \frac{K\lambda}{\beta cos\theta} \quad (2)$$

Where, K is a shape factor = 0.9, λ=1.5405 Å, θ is the Braggs diffraction angle and β is the FWHM of the broadening of diffraction line (in radian).

Table 1. Bragg's angle (2θ), Sinθ, interplanar space (d), Miller Indices (*hkl)* and lattice constant (a)

(hkl)	2θ	θ	$sin\theta$	$d_X\ (g/cm^3)$	α(Å)
(111)	18.218	9.109	0.1583	4.8656	8.4274
(220)	30.057	15.0285	0.2707	2.9706	8.9355
(311)	35.418	17.709	0.3041	2.5323	8.3890
(222)	38.669	19.3345	0.3310	2.3266	8.0595
(400)	43.101	21.5505	0.3673	2.0970	8.3880
(422)	53.442	26.721	0.4496	1.7131	8.3924
(511)	56.942	28.471	0.4767	1.6158	8.3959
(440)	62.506	31.253	0.5188	1.4847	8.3987

The X-ray density of $Cu_{(0.7)}Zn_{(0.3)}Fe_2O_4$ (CZK_7) ferrite nanoparticles was calculated by;

$$dx = {}^{8M}/_{Na^3} \quad (3)$$

Here 8 is a number of molecules for unit cell of spinel lattice, M is a Molecular weight in gram mole of the spinel and N = Avogadro number. The values of lattice constant, unit cell volume, X-ray density, and crystallite size were listed in table 2.

Table 2. Values of lattice constant (a), unit cell volume (V), X-ray density (dx), crystallite size (t).

α(Å)	V (Å)	$d_X\ (g/cm^3)$	t (nm)
8.422	597.53	5.330	24.17

It is evident from table 2 that, the lattice constant was found to be increased when zinc is doped in copper ferrite. The increase in lattice constant can be attributed to the larger ionic radius of Zn^{2+} ion (0.082 nm) which replaces a smaller Fe^{3+} ion (0.067 nm) [28]. The value of crystallite size (t) indicates the nanocrystalline nature of the prepared samples. Our results on lattice constant and other structural parameters are in a good agreement with the reported values [15].

4.2 Dielectric properties

The dielectric properties are studied by means of LCR Q meter and as a function of frequency at room temperature. The dielectric behavior of $Cu_{(0.7)}Zn_{(0.3)}Fe_2O_4$ (CZK_7) ferrite nanoparticles can be

explained on the basis of Maxwell-Wagner interfacial polarization which is in agreement with Koop's phenomenological theory. $CuFe_2O_4$ is an inverse spinel structure [29] with Cu^{2+} ions occupying octahedral [B] site by replacing Fe^{3+} ions which results in decrease in Fe^{3+} ions at octahedral [B] site. In the present study, the dielectric constant, dielectric loss and dielectric loss tangent were calculated using standard relations reported in the literature and their variation with respect to frequency was studied. The mesurements of the dielectric properties were recorded from 100 Hz- 1 MHz. By measuring capacitance C, the dielectric parameters were calculated.

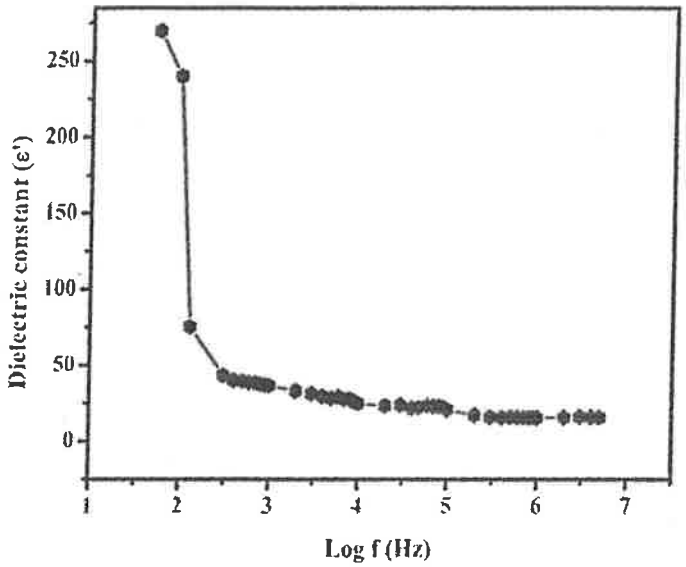

Figure 2. Dielectric constant (ε') of $Cu_{(0.7)}Zn_{(0.3)}Fe_2O_4$ (CZK_7) spinel ferrite nanoparticles

4.2.1 Dielectric constant (ε')

Figure 2 represents the variation of dielectric constant (ε') as a function of frequency. The plot shows exponential nature. At low frequencies, the dielectric constant is maximum and at higher frequencies, dielectric constant is minimum. This type of behaviour of dielectric constant was repeated in various spinel ferrite nanoparticles [30]. The observed decrease in dielectric constant with increase in frequency can be explained as at higher frequency any effect contributing a polarization is found to show lagging behind the applied field when frequency is increased beyond a certain frequency limit, the electron hopping cannot follow the electric field fluctuation and causes decreasing dielectric constant. These types of polarization are due to the inhomogeneous dielectric structure, like porosity and grain boundaries in the samples.

4.2.2 Dielectric loss (ε'')

Figure 3 represents the variation of dielectric loss as a function of frequency. The dielectric loss (ε'') decreases with increase in frequency as observed for dielectric constant (ε').

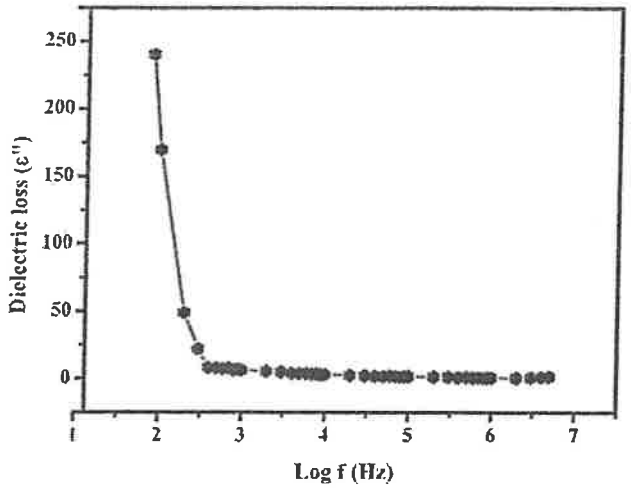

Figure 3. Dielectric loss (ε'') of $Cu_{(0.7)}Zn_{(0.3)}Fe_2O_4$ (CZK_7) spinel ferrite nanoparticles

At lower frequency the dielectric loss is maximum and at higher frequency the dielectric loss was recorded to be minimum which can be seen in figure 3.

4.2.3 Dielectric loss tangent (δ)

Figure 4 represents the frequency dependent dielectric loss tangent ($\tan\delta$) plot for mixed $Cu_{(0.7)}Zn_{(0.3)}Fe_2O_4$ (CZK_7) ferrite nanoparticles. Dielectric loss tangent plot exhibits similar nature as that of the dielectric constant (ε').

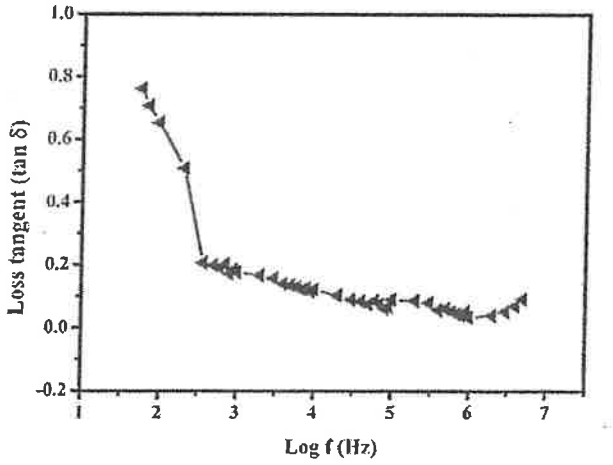

Figure 4. Dielectric loss tangent (δ) of $Cu_{(0.7)}Zn_{(0.3)}Fe_2O_4$ (CZK_7) spinel ferrite nanoparticles

Here, the dielectric loss tangent (δ) decreases with increase in frequency. At higher frequencies the dielectric loss tangent is minimum and at low frequencies the dielectric loss tangent (δ) was found to be maximum.

5. Conclusions

The mixed $Cu_{(0.7)}Zn_{(0.3)}Fe_2O_4$ (CZK_7) spinel ferrite nanoparticles have been successfully prepared by wet chemical sol-gel auto-combustion method. It was evident from XRD pattern that Bragg's angle (2θ) reflections are in very good agreement with the reported literature confirming the cubic spinel structure of (CZK_7). The Lattice constant (a) ~8.422 Å and other structural properties are in the reported range. The crystallite size (t) of the CZK_7 nanoparticles was measured ~24.17 nm which is a good achievement from the synthesis point of view for the present investigation. The dielectric constant (ε') decreases to a minimum value of frequency range (Hz) and remains almost constant for higher frequency range. Initially, the dielectric loss (ε'') was maximum and found to be decreases with increasing frequency. The dielectric loss tangent (δ) plot exhibits similar nature as that of the dielectric constant (ε') which decreases exponentially as a function of frequency. Considering the technological demands of the ferrite nanoparticles, overall investigation leads to a conclusion that the structural and dielectric study of $Cu_{(0.7)}Zn_{(0.3)}Fe_2O_4$ (CZK_7) spinel ferrite nanoparticles can be useful for high frequency applications.

Acknowledgement

One of the author S B Kale is thankful to Dr S M Patange, Department of Physics, Shrikrishna Mahavidyalaya, Gunjoti Tq. Omerga Osmanabad Maharashtra 413606 for providing LCR-Qmeter facility for the characterization of dielectric data for the present investigation.

References

[1] P. Saravanan, K. Jayamoorthy, S. Anandakumar, Fluorescence quenching of APTES by Fe2O3 nanoparticles–Sensor and antibacterial applications, Journal of Luminescence, 178 (2016) 241-248.
[2] K. K Rama, K. K Vijaya, R. Dachepalli, Structural and electrical conductivity studies in nickel-zinc ferrite, Advances in Materials physics and chemistry, 2012 (2012).
[3] S. Mansour, M. Abdo, F. Kzar, Effect of Cr dopant on the structural, magnetic and dielectric properties of Cu-Zn nanoferrites, Journal of Magnetism and Magnetic Materials, 465 (2018) 176-185.
[4] N. Gupta, A. Verma, S.C. Kashyap, D. Dube, Microstructural, dielectric and magnetic behavior of spin-deposited nanocrystalline nickel–zinc ferrite thin films for microwave applications, Journal of Magnetism and Magnetic Materials, 308 (2007) 137-142.
[5] P.B. Kharat, A.V. Humbe, J.S. Kounsalye, K.J.J.o.S. Jadhav, N. Magnetism, Thermophysical investigations of ultrasonically assisted magnetic nanofluids for heat transfer, 32 (2019) 1307-1317.
[6] N.P. Cook, P. Schwaninger, H. Widmer, Ferrite antennas for wireless power transfer, Google Patents, 2013.
[7] M. Shisode, P.B. Kharat, D.N. Bhoyar, V. Vinayak, M. Babrekar, K. Jadhav, Structural and multiferroic properties of Ba2+ doped BiFeO3 nanoparticles synthesized via sol-gel method, AIP Conference Proceedings, AIP Publishing LLC, 2018, pp. 030276.
[8] B.V. Prasad, K. Ramesh, A. Srinivas, Structural and magnetic studies of nano-crystalline ferrites MFe 2 O 4 (M= Zn, Ni, Cu, and Co) synthesized via citrate gel autocombustion method, Journal of superconductivity and Novel magnetism, 30 (2017) 3523-3535.
[9] M.V. Khedkar, S.A. Jadhav, S.B. Somvanshi, P.B. Kharat, K.J.S.A.S. Jadhav, Physicochemical properties of ambient pressure dried surface modified silica aerogels: effect of pH variation, 2 (2020) 1-10.
[10] A. Lipare, P. Vasambekar, A. Vaingankar, Effect of LiCl doping on dielectric behavior of copper–zinc ferrite system, Journal of magnetism and magnetic materials, 279 (2004) 160-172.
[11] S. Qamar, M.N. Akhtar, K.M. Batoo, E.H. Raslan, Structural and magnetic features of Ce doped Co-Cu-Zn spinel nanoferrites prepared using sol gel self-ignition method, Ceramics International, DOI (2020).

[12] M.V. Shisode, A.V. Humbe, P.B. Kharat, K.J.J.o.E.M. Jadhav, Influence of Ba 2+ on opto-electric properties of nanocrystalline BiFeO 3 multiferroic, 48 (2019) 358-367.
[13] N.K. Gupta, Y. Ghaffari, S. Kim, J. Bae, K.S. Kim, M. Saifuddin, Photocatalytic Degradation of Organic Pollutants over MFe 2 O 4 (M= Co, Ni, Cu, Zn) Nanoparticles at Neutral pH, Scientific reports, 10 (2020) 1-11.
[14] S.B. Somvanshi, S.R. Patade, D.D. Andhare, S.A. Jadhav, M.V. Khedkar, P.B. Kharat, P.P. Khirade, K.J.J.o.A. Jadhav, Compounds, Hyperthermic evaluation of oleic acid coated nano-spinel magnesium ferrite: enhancement via hydrophobic-to-hydrophilic surface transformation, DOI (2020) 155422.
[15] M.A. Yousuf, S. Jabeen, M.N. Shahi, M.A. Khan, I. Shakir, M.F. Warsi, Magnetic and electrical properties of yttrium substituted manganese ferrite nanoparticles prepared via micro-emulsion route, Results in Physics, 16 (2020) 102973.
[16] P. Palade, C. Comanescu, A. Kuncser, D. Berger, C. Matei, N. Iacob, V. Kuncser, Mesoporous Cobalt Ferrite Nanosystems Obtained by Surfactant-Assisted Hydrothermal Method: Tuning Morpho-structural and Magnetic Properties via pH-Variation, Nanomaterials, 10 (2020) 476.
[17] A. Singh, P. Chauhan, Structural, electrical and optical properties of Mn0. 2Co0. 8Fe2O4 nano ferrites, Materials Today: Proceedings, DOI (2020).
[18] S.R. Patade, D.D. Andhare, P.B. Kharat, A.V. Humbe, K.J.C.P.L. Jadhav, Impact of crystallites on enhancement of bandgap of Mn1-xZnxFe2O4 ($1 \geq x \geq 0$) nanospinels, 745 (2020) 137240.
[19] H. Shashidharagowda, S.N. Mathad, Effect of incorporation of copper on structural properties of spinel nickel manganites by co-precipitation method, Materials Science for Energy Technologies, 3 (2020) 201-208.
[20] P.B. Kharat, A.R. Chavan, A.V. Humbe, K.J.J.o.M.S.M.i.E. Jadhav, Evaluation of thermoacoustics parameters of CoFe 2 O 4–ethylene glycol nanofluid using ultrasonic velocity technique, 30 (2019) 1175-1186.
[21] M. Almessiere, Y. Slimani, H. Güngüneş, V. Kostishyn, S. Trukhanov, A. Trukhanov, A. Baykal, Impact of Eu3+ ion substitution on structural, magnetic and microwave traits of Ni–Cu–Zn spinel ferrites, Ceramics International, DOI (2020).
[22] D. Allam, S. Bennici, L. Limousy, S. Hocine, Improved Cu-and Zn-based catalysts for CO2 hydrogenation to methanol, Comptes Rendus Chimie, 22 (2019) 227-237.
[23] J. Liu, Y. Liu, W. Yan, D. Yang, J. Fan, W. Huang, Effect of zinc source on the ethanol synthesis from syngas over a slurry CuZnAl catalyst, International Journal of Hydrogen Energy, DOI (2020).
[24] W. Zhang, A. Sun, X. Zhao, X. Pan, Y. Han, N. Suo, L. Yu, Z. Zuo, Structural and magnetic properties of Ni–Cu–Co ferrites prepared from sol-gel auto combustion method with different complexing agents, Journal of Alloys and Compounds, 816 (2020) 152501.
[25] S. Kanagesan, M. Hashim, S. AB Aziz, I. Ismail, S. Tamilselvan, N.B. Alitheen, M.K. Swamy, B. Purna Chandra Rao, Evaluation of antioxidant and cytotoxicity activities of copper ferrite (CuFe2O4) and zinc ferrite (ZnFe2O4) nanoparticles synthesized by sol-gel self-combustion method, Applied Sciences, 6 (2016) 184.
[26] A. Abdeen, Electric conduction in Ni–Zn ferrites, Journal of magnetism and magnetic materials, 185 (1998) 199-206.
[27] A.R. Lamani, H. Jayanna, P. Parameswara, R. Somashekar, Microcrystalline parameters of Cu-Zn ferrites using X-ray line profile analysis, DOI (2009).
[28] R. Kulkarni, V. Patil, Magnetic ordering in Cu-Zn ferrite, Journal of Materials Science, 17 (1982) 843-848.
[29] A. Gholizadeh, E. Jafari, Effects of sintering atmosphere and temperature on structural and magnetic properties of Ni-Cu-Zn ferrite nano-particles: Magnetic enhancement by a reducing atmosphere, Journal of Magnetism and Magnetic Materials, 422 (2017) 328-336.
[30] A. Sattar, S.A. Rahman, Dielectric properties of rare earth substituted Cu–Zn ferrites, physica status solidi (a), 200 (2003) 415-422.

Journal of Physics: Conference Series

Low-temperature synthesis, structural characteristic of magnesium ferrite

Low-temperature synthesis, structural characteristic of magnesium ferrite

Vinay Mahale[1], A V Raut[2], V K Surashe[3], S R Nimbhore[4], R G Dorik[2] and D R Shengule[2]

[1]Department of Physics, Dr. Babasaheb Ambedkar Marathwada University, Aurangabad 431004 India

[2]Department of physics, Vivekanand Art's and Sardar Dalipsing Commerce and Science College, Aurangabad 431001 India

[3]Department of physics, Arts, Science & Commerce College, Badnapur, Jalna 431202 India

[4]Department of Physics, Adv. B.D. Hambarde Mahavidyalaya, Ashti, (M. S.), India

Corresponding author email : drrgdorik@gmail.com

Abstract. The present paper deals with the synthesis and the structural characterization of magnesium ferrite ($MgFe_2O_4$) the synthesis of $MgFe_2O_4$ was carried out by well-known sol-gel auto-combustion method in which citric acid was used as a chelating agent. The as obtained powder of $MgFe_2O_4$ was then annealed at 500° C for 4 h to improve the crystallinity and remove the impurities. The annealed powder of $MgFe_2O_4$ was then subjected to X-ray diffraction study in order to know the phase purity and crystal structure. The X-ray diffraction pattern (XRD) reveals the presence of those reflections which belongs to cubic spinel structure. The analysis of XRD pattern proves that the prepared $MgFe_2O_4$ powder is nanocrystalline in nature and possesses single phase cubic spinel structure. Using the XRD data the structural parameters like lattice constant, unit cell volume, X-ray density, hopping length, tetra edge and octa edge etc. structural parameters were determined. The obtained structural parameters are in good agreement to that reported in the literature. The crystallite size was also obtained by standard Sherrer's formula and was found to be 22 nanometre. Thus, the nanocrystalline nature of $MgFe_2O_4$ was obtained through sol-gel auto-combustion method and the X-ray diffraction study reveals the single phase cubic spinel structure.

1. Introduction

The magnetic materials in which iron oxide and metal oxide in particular ratio present are known as ferrites. Ferrites are ferromagnetic in nature as proposed by L Neel [1]. They possess very interesting electrical as well as magnetic properties. By virtue of combined property of electrical insulator and magnetic conductor ferrites [2] are recognised as one of the best magnetic materials to be applied in several fields. They possess high electrical resistivity [3], low eddy current and dielectric losses [4], high saturation magnetization [5] etc. important properties which make them many technological applications. On the basis of crystal structure, ferrite are grouped in to three main classes namely

spinel ferrite [6], garnet [7] and hexagonal ferrite [8]. They can be easily synthesised by various preparative techniques like ceramic [9], chemical co-precipitation [10], hydrothermal [11], sol-gel [12] etc.. Currently, nanocrystalline spinel ferrite [13] has attracted the attention of various researchers due to their nanoscale dimensions [14], high chemical stability [15], and large surface to volume ratio [16], better homogeneity and easy preparation [17]. The nanocrystalline spinel ferrite finds application in the field of sensors [18], catalyst [19], drug delivery [20], water purification [21]. The spinel ferrites are characterised by the formula $MgFe_2O_4$ in which M represent divalent metal ion like Mg^{2+}, Co^{2+}, Ni^{2+}, Zn^{2+}, Fe^{2+}, Mn^{2+}, etc. The structure of spinel ferrite is cubic spinel which space group fd_3m. The spinel lattice consists of two sites i.e. tetrahedral (A)-site and octahedral [B]-site. These two sites can occupy cations of different size elements bringing wide variation in electrical and magnetic properties. The synthesis method also plays an important role in governing the properties of spinel ferrite. The wet chemical methods in particular sol-gel auto-combustion method are a unique method which possess nanoscale powder of high quality. Among the various spinel ferrite, magnesium ferrite $MgFe_2O_4$ [22] is a well-known ferrite and is rarely studied. It possesses partially inverse structure which depends on synthesis method and synthesis conditions. In the literature very few reports are available for the synthesis and characterisation of $MgFe_2O_4$ [23]. Considering the importance of $MgFe_2O_4$ in various technological applications, it was decided to study the nanocrystlline magnesium ferrite and to evaluate their structural properties. In this paper we report our results on the synthesis and structural characterizations of magnesium ferrite.

2. Experimental

2.1 Raw Materials

Nanocrystalline spinel structured Mg-ferrite ($MgFe_2O_4$) has been prepared by sol-gel auto-combustion method using citric acid as a fuel. AR grade magnesium nitrate ($Mg(NO_3)_2$), ferric nitrate ($Fe(NO_3)_3 \cdot 9H_2O$) and citric acid ($C_6H_8O_7$) were used for the synthesis. As a part of synthesis method, an anhydrous Ammonia compound of nitrogen and hydrogen with the formula NH_3 was considered for maintaining pH of the solution.

2.2 Synthesis Method

In this wet chemical particular sol-gel auto-combustion method, metal nitrate to citric acid ratio was taken as 1:3. This was done by mixing of ($Mg(NO_3)_2$) granules in to double distilled water and clear solution of magnesium nitrate was formed. Similarly, ($Fe(NO_3)_3 \cdot 9H_2O$) granules was mixed in a double distilled water and second solution of ferric nitrate was obtained. Citric acid [24] was formed by adding the ($C_6H_8O_7$) granules in double distilled water and we consider this as a fuel for the sol-gel auto-combustion reaction. Ferric nitrate and magnesium nitrate solutions were mixed together and a third solution of citric acid was added in proportion maintaining metal nitrate to fuel ratio of 1:3. The mixed solution was stirred and heated continuously on hot-plate magnetic stirrer at 70° C for the slow evaporation of excess water, which makes the proper reaction to be done within the mixed solution state. Meanwhile, Ammonia [25] was used to maintain the pH of the solution at 8, and it was added drop by drop with the help of burette in the mixed solution placed on hot-plate magnetic stirrer. Over the constant stirring and heating, the transparent sol was obtained which was further heated to 110° C for accelerating the chemical reaction within the metal nitrates. The concluding part of the sol-gel takes place at a particular temperature and citrate-nitrate gel reaction takes place. An auto-combustion starts with a final ignition state and a dry-gel form of all constituents starts burning by itself. This will give us a powder form of Mg-ferrite which was characterised thereafter.

3. Characterization

3.1 X-Ray Diffraction

The room temperature X-ray diffraction pattern of nanocrystalline Mg-ferrite ($MgFe_2O_4$) was taken by using Cu-kα radiation (λ = 1.5405 Å) on Philips PW-1730 X-ray diffractometer. The X-ray diffraction pattern was recorded in the 2θ range of 20° to 80° with a scanning rate of 0.02 deg/s. All the major Bragg's reflections of nanocrystalline Mg-ferrite were recorded for the analysis of structural parameters.

4. Results and discussion

4.1 Structural Properties

The prepared magnesium ferrite ($MgFe_2O_4$) was studied for a structural characterization by X-ray diffraction method. The X-ray diffraction method is useful in determining the phase purity, size of the particles and for the determination of various structural parameters. The following table 1 represents the Miller indices (hkl), Brag's angle, interplanner spacing (d) and intensity of the various reflections evolved in the X-ray diffraction pattern.

Table 1. Miller Indices (*hkl*), Bragg's angle (2θ), Sin θ, $sin\,\theta/\lambda$ interplannar spacing (d), and Intensity of various reflections

(hkl)	2θ	θ	$sin\theta$	$sin\,\theta/\lambda$	d(Å)	I (a.u.)	I/I_0
(220)	30.309	15.15	0.261	0.1697	2.9465	4471.8	65.4
(311)	35.658	17.83	0.306	0.1987	2.5158	6842.6	100.0
(222)	37.859	18.93	0.324	0.2106	2.3744	3905.3	57.1
(400)	43.256	21.63	0.369	0.2392	2.0899	4666.5	68.2
(422)	53.675	26.84	0.451	0.2930	1.7062	4264.2	62.3
(511)	57.198	28.60	0.479	0.3107	1.6092	4877	71.3
(440)	62.754	31.38	0.521	0.3380	1.4794	5330.6	77.9
(620)	71.166	35.58	0.582	0.3777	1.3238	4112	60.1
(533)	74.298	37.15	0.604	0.3920	1.2755	4219.5	61.7

In the obtained XRD pattern the maximum intensity was observed for the (311) reflection and same reflection is used for determine the crystallite size (t). It can be observed from the table 1 that with increasing Brag's angel the interplanner spacing (d) decreases. The reflections occur at (220), (311), (222), (400), (422), (511), (440), (620) and (533) within the range of 20° to 80° [26]. No additional reflections other than these were observed in XRD pattern. In the cubic spinel structure the samples shows all these reflections. Thus, it can be concluded from XRD data that, the prepared Mg-ferrite possesses single phase cubic spinel structure [27].

4.2 Crystallite size (t) nm

The crystallite size (t) was calculated by using Debye-Scherrer method, which is mentioned by eq. [28] ;

$$t = \frac{K\lambda}{\beta cos\theta} \quad (1)$$

The crystallite size (t) of magnesium ferrite ($MgFe_2O_4$) sample was found to be 22 nanometre, thus confirming the nanocrystalline nature.

4.3 Lattice constant (a) Å

The lattice constant (a) of $MgFe_2O_4$ was calculated by the following relation in eq. [22];

$$a = d_{hkl}(h^2 + k^2 + l^2)^{\frac{1}{2}} \quad (2)$$

The lattice constant (a) was obtained to be 8.341 Å, which is in good agreement with the literature value.

Table 2. lattice parameter α(Å), X-ray density $d_X(g/cm^3)$, Volume V, and molecular weight $^{gm}/_{mol}$ of nanocrystalline $MgFe_2O_4$

Composition x	α(Å)	$d_X(g/cm^3)$	V (Å^3)	Mol. Wt. $^{gm}/_{mol}$
0.0	8.3413	4.5770	580.4	199.9590

4.4 X-ray density (d_X)

The X-ray density (d_X) was calculated by the following relation (3) [29] the X-ray density was obtained to be 4.577 (g/cm^3). The values of crystallite size lattice constant, unit cell volume and X-ray density are listed in table 2.

$$dx = {}^{8M}/_{Na^3} \quad (3)$$

4.5 Hopping Length (L_A ; L_B)

The hopping length (L_A ; L_B) for the present $MgFe_2O_4$ samples was calculated by using the following relations [30].

$$L_A = a_O \frac{\sqrt{3}}{4} \quad (4)$$

$$L_B = a_O \frac{\sqrt{2}}{4} \quad (5)$$

4.6 Tetra edge (D_{AXE}) and octa edge (D_{BXE})

The values of (L_A ; L_B) are listed in table 3. The other structural parameters like tetrahedral bonds D_{AL} octahedral bond D_{BL}, tetra edge D_{AXE} and octa edge D_{BXE} was calculated by the following relations [31], and their values are given in table 3.

$$d_{AX} = a\sqrt{3u}\left(u - \frac{1}{4}\right) \quad (6)$$

$$d_{BX} = a\left(3u^2 - \frac{11}{4}u + \frac{43}{64}\right)^{\frac{1}{2}} \quad (7)$$

$$d_{AXE} = a\sqrt{2}\left(2u - \frac{1}{2}\right) \quad (8)$$

$$d_{BXE} = a\sqrt{2}\,(1 - 2u) \quad (9)$$

$$d_{BXEu} = a\left(4u^2 - 3u + \frac{11}{16}\right)^{\frac{1}{2}} \quad (10)$$

All the values of structural parameters obtained for the present mg are in confirmation with reported values.

Table 3. Hopping length (L_A, L_B), tetrahedral bond (d_{AX}), octahedral bond (d_{BX}), tetra-edge (d_{AXE}), and octa-edge (d_{BXEu}) for nanocrystalline $MgFe_2O_4$

Composition x	L_A(Å)	L_B(Å)	d_{AX}(Å)	d_{BX}(Å)	d_{AXE}(Å)	d_{BXE}(Å)	d_{BXEu}(Å)
0.00	3.6119	2.9491	1.8926	2.0365	3.0906	2.8075	2.9508

5. Conclusions

In the present study, we have successfully prepared $MgFe_2O_4$ nanocrystalline nature, using sol-gel auto-combustion method. The crystallite size of the prepared $MgFe_2O_4$ was recorded as 22 nanometre. From the XRD data values it is cleared that; the prepared $MgFe_2O_4$ belongs to single phase cubic spinel structure. Also, it was evident from XRD pattern that Bragg's angle (2θ) reflections are in very good agreement with the reported literature. X-ray density (d_X) was obtained as 4.577 (g/cm^3). The lattice constant α was reported as 8.3413 (Å) and other structural parameters are in the reported range. The hopping length (L_A ; L_B) as well as tetrahedral bonds D_{AL} octahedral bond D_{BL}, tetra edge D_{AXE} and octa edge D_{BXE} for the present $MgFe_2O_4$ samples are according to the calculations.

6. Acknowledgement

One of the author Vinay Mahale is thankful to Prof. K M Jadhav, Department of Physics, Dr. Babasaheb Ambedkar Marathwada University, Aurangabad 431004 India for providing synthesis and charectarization facilities for the present investigation.

7. References

1. Néel, L., *Some new results on antiferromagnetism and ferromagnetism.* Reviews of Modern Physics, 1953. **25**(1): p. 58.
2. Mulushoa, S.Y., et al., *Synthesis of Spinel MgFe2O4 Ferrite Material and Studying its Structural and Morphological Properties Using Solid State Method.* Chemical Science, 2017. **6**(4): p. 653-661.
3. Abraham, A.G., et al., *Enhanced magneto-optical and photo-catalytic properties of transition metal cobalt (Co2+ ions) doped spinel MgFe2O4 ferrite nanocomposites.* Journal of Magnetism and Magnetic Materials, 2018. **452**: p. 380-388.
4. Sivakumar, N., et al., *Electrical and magnetic behaviour of nanostructured MgFe2O4 spinel ferrite.* Journal of Alloys and Compounds, 2010. **504**(2): p. 395-402.

5. Chen, D., Y. Zhang, and C. Tu, *Preparation of high saturation magnetic MgFe2O4 nanoparticles by microwave-assisted ball milling.* Materials Letters, 2012. **82**: p. 10-12.
6. Wang, X., et al., *Characterization of microstructure and magnetic properties for Co2+ ions doped MgFe2O4 spinel ferrites.* Materials Today Communications, 2020: p. 101414.
7. Zheng, H., et al., *Intrinsic Lithiophilicity of Li–Garnet Electrolytes Enabling High-Rate Lithium Cycling.* Advanced Functional Materials, 2020. **30**(6): p. 1906189.
8. Yasmin, N., et al., *Impact of Ho-Ni substitution on structural, morphological and dielectrical characteristics of BaFe12O19 M-type hexagonal ferrite.* Physica B: Condensed Matter, 2020. **581**: p. 411950.
9. Dastjerdi, O.D., H. Shokrollahi, and H. Yang, *The enhancement of the Ce-solubility limit and saturation magnetization in the Ce0. 25BixPryY2. 75-x-yFe5O12 garnet synthesized by the conventional ceramic method.* Ceramics International, 2020. **46**(3): p. 2709-2723.
10. Thambidurai, S., et al., *Enhanced bactericidal performance of nickel oxide-zinc oxide nanocomposites synthesized by facile chemical co-precipitation method.* Journal of Alloys and Compounds, 2020: p. 154642.
11. Mo, Y., et al., *Ethanol-sensing properties of α-MoO3 nanobelts synthesized by hydrothermal method.* Journal of Alloys and Compounds, 2020. **812**: p. 152166.
12. Uke, S.J., et al., *Sol-gel citrate synthesized Zn doped MgFe2O4 nanocrystals: A promising supercapacitor electrode material.* Materials Science for Energy Technologies, 2020.
13. Anantharamaiah, P., et al., *Enhancing the catalytic activity of recyclable nanocrystalline NiFe2O4 by replacing Ni by Cu.* Ceramics International, 2020. **46**(1): p. 1220-1226.
14. Morais, V., et al., *Synthesis of manganese ferrite from spent Zn–MnO2 batteries and its application as a catalyst in heterogeneous photo-Fenton processes.* Journal of Environmental Chemical Engineering, 2020. **8**(3): p. 103716.
15. Amiri, M., M. Salavati-Niasari, and A. Akbari, *Magnetic nanocarriers: evolution of spinel ferrites for medical applications.* Advances in Colloid and Interface Science, 2019. **265**: p. 29-44.
16. Lakshmi, V., et al. *Structural and Magnetic Studies of Zinc Substituted Cobalt Ferrite Nanoparticles prepared by Sol–Gel Technique.* in *IOP Conference Series: Materials Science and Engineering.* 2019. IOP Publishing.
17. Saidani, M., et al., *Unexpected magnetic properties explained by the homogeneity of mixed ferrites.* Journal of Alloys and Compounds, 2017. **695**: p. 183-193.
18. Wu, K., J. Li, and C. Zhang, *Zinc ferrite based gas sensors: A review.* Ceramics International, 2019. **45**(9): p. 11143-11157.
19. Das, I., et al., *Synthesis of bimetallic iron ferrite Co0. 5Zn0. 5Fe2O4 as a superior catalyst for oxygen reduction reaction to replace noble metal catalysts in microbial fuel cell.* International Journal of Hydrogen Energy, 2018. **43**(41): p. 19196-19205.
20. Dey, C., et al., *Improvement of drug delivery by hyperthermia treatment using magnetic cubic cobalt ferrite nanoparticles.* Journal of Magnetism and Magnetic Materials, 2017. **427**: p. 168-174.
21. Reddy, D.H.K. and Y.-S. Yun, *Spinel ferrite magnetic adsorbents: alternative future materials for water purification?* Coordination Chemistry Reviews, 2016. **315**: p. 90-111.
22. Somvanshi, S.B., et al., *Hyperthermic evaluation of oleic acid coated nano-spinel magnesium ferrite: enhancement via hydrophobic-to-hydrophilic surface transformation.* Journal of Alloys and Compounds, 2020: p. 155422.
23. Kumar, S. and K. Sreenivas. *Electrical conductivity of magnesium ferrite prepared by sol-gel auto combustion technique.* in *AIP Conference Proceedings.* 2019. AIP Publishing LLC.
24. Li, J., et al., *Electrospun Fe2O3 nanotubes and Fe3O4 nanofibers by citric acid sol-gel method.* Journal of the American Ceramic Society, 2017. **100**(12): p. 5460-5470.

25. Deepapriya, S., et al. *Effect of pH on structural, morphological, photoacoustic and magnetic properties of NiLaFe2O4 ferrite nanocomposites for gas sensing applications*. in *AIP Conference Proceedings*. 2020. AIP Publishing LLC.
26. Khalaf, K.A., et al., *Effects of Zn Substitution on Structure Factors, Debye-Waller Factors and Related Structural Properties of the Mg1-xZnxFeNiO4 Spinels*. Advances in Materials, 2019. **8**(2): p. 70.
27. Meidanchi, A., *Mg (1-x) CuxFe2O4 superparamagnetic nanoparticles as nano-radiosensitizer agents in radiotherapy of MCF-7 human breast cancer cells*. Nanotechnology, 2020. **31**(32): p. 325706.
28. Batoo, K.M., et al., *Investigation of electrical, magnetic, and optical properties of silver-substituted magnesium–manganese ferrite nanoparticles*. Journal of Materials Science: Materials in Electronics, 2020: p. 1-9.
29. Jadhav, G.L., et al., *Effect of magnesium substitution on the structural, morphological, optical and wettability properties of cobalt ferrite thin films*. Physica B: Condensed Matter, 2019. **555**: p. 61-68.
30. Vishwaroop, R. and S.N. Mathad, *Synthesis, Structural, WH Plot and Size-Strain Analysis of Nano Cobalt Doped MgFe2O4 Ferrite*. Science of Sintering, 2020. **52**(3).
31. Shedam, R., et al., *Structural and mechanical properties of nanograined magnesium ferrite produced by oxalate coprecipitation method*. International Journal of Self-Propagating High-Temperature Synthesis, 2017. **26**(1): p. 75-79.